Earth and Planetary Science Letters ••• (••••) ••••••

Contents lists available at ScienceDirect

Earth and Planetary Science Letters

www.elsevier.com/locate/epsl

# Air-sea coupling shapes North American hydroclimate response to ice sheets during the Last Glacial Maximum

Dillon J. Amaya [a,*], Alan M. Seltzer [b], Kristopher B. Karnauskas [a,c], Juan M. Lora [d], Xiyue Zhang [e], Pedro N. DiNezio [c]

[a] Cooperative Institute for Research in Environmental Sciences, University of Colorado Boulder, United States of America
[b] Woods Hole Oceanographic Institution, United States of America
[c] Department of Atmospheric and Oceanic Sciences, University of Colorado Boulder, United States of America
[d] Department of Earth and Planetary Sciences, Yale University, United States of America
[e] Department of Earth and Planetary Sciences, Johns Hopkins University, United States of America

ARTICLE INFO

*Article history:*
Received 17 May 2021
Received in revised form 23 September 2021
Accepted 26 October 2021
Available online xxxx
Editor: Y. Asmerom

*Keywords:*
Last Glacial Maximum
hydroclimate
paleoclimate
climate modeling
air-sea interactions

ABSTRACT

The Western U.S. is vulnerable to hydrological stress, and insights from past climate periods are helpful for providing historical benchmarks for future climate projections. Myriad evidence from coupled models and paleoclimatic proxies suggests a major reorganization of west coast hydroclimate during the Last Glacial Maximum (LGM, ~17–25 ka), such that the Southwest U.S. was wetter than modern day and the Pacific Northwest was drier. Yet the fundamental mechanisms underlying these hydroclimatic shifts remain unclear. Here, we employ a suite of targeted model simulations to probe the influence of LGM Northern Hemisphere ice sheets on west coast atmospheric dynamics. Whereas previous modeling studies have suggested that the southward shift of LGM west coast precipitation was driven only by the mechanical steering of atmospheric circulation by elevated ice sheet topography, we find this to be an artifact of earlier simulations that neglected realistic air-sea interaction. Instead, our simulations indicate that ice sheet albedo induced a pattern of North Pacific sea surface temperatures, reinforced by ocean-atmosphere feedbacks, that shifted the large-scale atmospheric circulation as well as the latitudinal distribution of west coast precipitation southward during the LGM. Crucially, we find that atmosphere-ocean feedbacks that sustained this ice sheet albedo-induced temperature pattern in the LGM could drive similar hydroclimatic changes today.



## 1. Introduction

The hydroclimate of western North America is heavily influenced by intermittent wintertime storms ("atmospheric rivers") that can produce extreme precipitation, especially when these storms encounter substantial orographic features. For California, in particular, annual water availability hinges on the occurrence of just a handful of such atmospheric river events (Ralph and Dettinger, 2011). This region's acute vulnerability to climate variability and change is exacerbated by its growing human population. Therefore, understanding the fundamental drivers of hydroclimatic change over the west coast of the United States is essential for predicting the future habitability and agricultural viability of this region.

Large amplitude shifts in past climate, beyond the relatively brief instrumental record, provide essential insights into such projections. In this regard, the Last Glacial Maximum (LGM) serves as a useful test case of a relatively recent stable climate state that (a) was substantially different than our present climate and (b) for which we have reasonable constraints on important boundary conditions including orbital geometry, greenhouse gas (GHG) concentrations, sea level, ice volume, etc. To effectively leverage the LGM as a testbed for understanding future change, however, it is necessary to disentangle the climate impacts of forcings that are presently changing (e.g., GHG concentrations) from those that are not (e.g., continental ice sheets).

It has long been suggested that a major non-GHG driver of LGM atmospheric circulation change was the large topographic extent of the ice sheets over North America (Fig. 1). Ice sheet forcing has been linked to the dramatic reorganization of west coast hydroclimate during the LGM (Anderson et al., 1988; Broccoli and Manabe, 1987; Cook and Held, 1988; Wong et al., 2016; Yanase and Abe-Ouchi, 2010), which is suggested to have been considerably wetter

* Corresponding author.
*E-mail address:* dillon.amaya@colorado.edu (D.J. Amaya).

https://doi.org/10.1016/j.epsl.2021.117271
0012-821X/

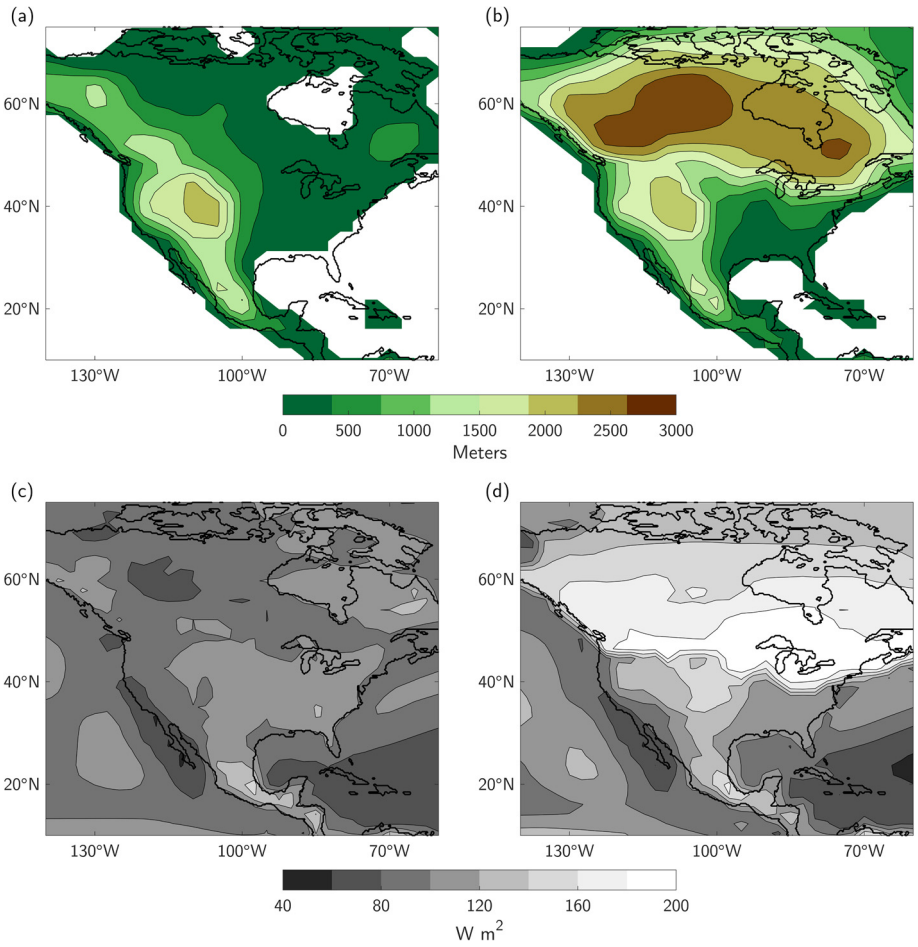


**Fig. 1.** Ice sheet characteristics in our CESM1 simulations. (a)–(b) Surface geopotential divided by 9.8 m/s$^2$ (meters) and (c)–(d) annual mean upward shortwave radiation at the top of the atmosphere (W m$^{-2}$) in our CTL (left column) and LGM (right column) simulations. LGM$_{Full}$ and WM simulations have the ice sheet surface properties of (b) and (d) (i.e., tall and bright). GM simulations have the ice sheet surface properties of (b) and (c) (i.e., tall and dark). WP simulations have the ice sheet surface properties of (a) and (d) (i.e., flat and bright).

than present throughout the southwestern U.S. by a preponderance of general circulation model (GCM) simulations and paleoclimate proxy reconstructions (Anderson et al., 1988; Bartlein et al., 2011; Benson et al., 2011; Ibarra et al., 2014; Kirby et al., 2013; Lachniet et al., 2014; Lemons et al., 1996; Lora et al., 2017; Maher et al., 2014; Oster et al., 2015; Owen et al., 2003; Reheis et al., 2012; Seltzer et al., 2019; Thompson et al., 1999). In particular, coupled model simulations nearly universally indicate a north-south dipole in LGM-to-present precipitation change, such that western North America was wetter in the south and drier in the north (Lora, 2018; Oster et al., 2015).

While models and (to a lesser extent) proxies broadly agree on the existence of this north-south LGM-to-present precipitation dipole response, the physical mechanisms that drove this shift remain an open question. One leading hypothesis is that the North Pacific jet stream was either split or deflected southward, so that extratropical storms and moisture transport occurred further south (Lora et al., 2017). Many studies indicate that the southward deflection of the North Pacific jet may have been the result of mechanical forcing imposed by North American ice sheets, which covered much of modern day Canada and stood ~3 km taller than the present day land surface (Anderson et al., 1988; Bartlein et al., 1998; Bromwich et al., 2004; Cook and Held, 1988; Kim et al., 2008; Kutzbach and Wright, 1985; Manabe and Broccoli, 1985). Other studies point to the dominant influence of high latitude cooling induced by the high albedo of ice sheets (Bhattacharya et al., 2017; Manabe and Broccoli, 1985; Morrill et al., 2018; Roberts et al., 2019; Yanase and Abe-Ouchi, 2010).

Recently, Roberts et al. (2019) found that wintertime atmospheric stationary wave patterns over the North Pacific during the LGM are primarily driven by ice sheet topography, but are enhanced by ice sheet albedo. In contrast, they showed that summertime stationary wave patterns are mainly driven by diabatic heating from the ice sheet albedo with little contribution from ice sheet topography. In addition, they suggested that ocean dynamics also play a key role in persisting atmospheric circulation anomalies from the summer into the winter. This is consistent with other previous analyses that have broadly implicated ocean-atmosphere coupling as an important factor in modulating the overall response to LGM boundary conditions (DiNezio et al., 2018; Löfverström et al., 2014; Yanase and Abe-Ouchi, 2010).

While these recent studies have provided significant insight into how the different characteristics of the Laurentide and Cordilleran ice sheets may have influenced North Pacific atmospheric circulation, several important questions remain. First, how do different ice sheet-driven stationary wave changes (e.g., Roberts et al., 2019) map onto potential shifts in the North Pacific jet stream? Following from this, do different responses of the zonal circulation to ice sheet topography and ice sheet albedo lead to different hydroclimate shifts along western North America? Additionally, what are the specific ocean dynamical processes and air-sea feedbacks that modulate the seasonally varying response

**Table 1**
List of the CESM1 experiments used in this study. Crosses indicate the boundary condition has been modified following PMIP3 protocols. All boundary conditions have been applied globally. The availability of dynamical ocean model (DOM), slab ocean model (SOM), or AGCM data is noted in parentheses. The equilibration period for each DOM run is shown in the far right column. The column second from right indicates the additional integration period used for calculating climatologies once each DOM run had reached close to radiative equilibrium. Each SOM and AGCM simulation was spun-up for 10 yrs, and integrated for an additional 100 yrs for calculating climatologies. See DiNezio et al. (2018) for complete details regarding the initial conditions and the boundary conditions.

| | GHGs | Orbit | Land mask & bathymetry | Topography | Albedo | Duration (yrs) | Equilibration (yrs) |
|---|---|---|---|---|---|---|---|
| $LGM_{Full}$ (DOM) | X | X | X | X | X | 600 | 500 |
| White Mountain (DOM, SOM, AGCM) | | | | X | X | 400 | 700 |
| Green Mountain (DOM, SOM, AGCM) | | | | X | | 200 | 100 |
| White Plains (DOM) | | | | | X | 400 | 500 |

of the North Pacific atmosphere to difference ice sheet boundary conditions?

Here we address these questions by exploring a suite of model simulations (Table 1) conducted with the Community Earth System Model version 1.2 (CESM1) to uncover the drivers and mechanisms of North American west coast hydroclimate change during the LGM, with targeted experiments to distinguish the mechanical (e.g., orographic) and thermodynamic (e.g., albedo-driven) impacts of large continental ice sheets on North Pacific atmospheric circulation. In addition, we build upon Roberts et al. (2019) and others by including a comprehensive range of ocean model complexities, which allow us to directly diagnose the specific ocean-atmosphere interactions and ocean circulation changes that are most relevant to the overall climate response.

## 2. Data and methods

### 2.1. Climate model simulations

The climate model simulations used in this study were conducted by DiNezio et al. (2018). Here, we will provide a broad overview of the major model components, as well as a brief summary of the LGM boundary conditions applied to our various simulations. However, we direct readers to the Supplementary Materials Sections S3–S5 in DiNezio et al. (2018) for a complete description of the climate model components and boundary conditions. Our simulations were carried out using the CESM1 global climate model, which consists of the Community Atmospheric Model version 5 (CAM5; ∼2° horizontal resolution with 30 vertical pressure levels). CAM5 is coupled to a full-depth ocean model—the Parallel Ocean Program version 2 (POP2)—featuring ∼1° horizontal resolution, with increased meridional resolution of ∼1/3° in the tropics, and 60 vertical levels. Additionally, CESM1 features the Community Land Model version 4 (CLM4) with ∼2° horizontal resolution.

We compare four sets of equilibrated CESM1 experiments with varying degrees of ocean complexity. They include: (1) A fully forced LGM experiment ($LGM_{Full}$) with all major glacial boundary conditions (GHGs, sea level, orbital, ice sheet topography and albedo, etc.) prescribed following the Paleoclimate Modeling Intercomparison Project Phase III (PMIP3) LGM protocols at 21,000 yrs ago, (2) A "White Mountain" (WM) simulation that includes all of the LGM ice sheet boundary conditions (e.g., extent, elevation, surface properties), but with the remaining boundary conditions (GHGs, orbit, sea level) set to pre-industrial levels, (3) A "Green Mountain" (GM) simulation that includes identical topography to the WM, but with land surface properties and the remaining boundary conditions set to pre-industrial values, and (4) A pre-industrial control simulation (CTL) with boundary conditions following the PMIP3 pre-industrial protocols. Fig. 1 further illustrates the different LGM and CTL land surface properties used in our experiments.

Ice sheet topography and glacier extent in each of our simulations were prescribed following PMIP3 protocols, which combine three different ice sheet reconstructions (Abe-Ouchi et al., 2015). Otto-Bliesner et al. (2006) showed that the simulated LGM climate in earlier versions of CESM could be sensitive to the choice of ice sheet reconstruction. However, our LGM results do not significantly differ when repeating our analysis using an updated ice sheet reconstruction from ICE-6G_C.

The WM and GM experiments include repeated simulations with an atmospheric model that is: (a) uncoupled from the ocean model (AGCM only; i.e., intrinsic atmospheric variability only), (b) coupled to a fixed, 50 m depth slab ocean model (SOM; i.e., no ocean circulation, but ocean-atmosphere interactions possible), and (c) fully coupled to a dynamical ocean model (DOM). In our AGCM experiments, global sea surface temperature (SST) and sea ice extent were prescribed with climatological values from the CTL. Differences among the SOM/DOM and AGCM configurations highlight the role of interactive ocean processes in shaping the overall climate response in the respective GM/WM experiments, while differences between the DOM and SOM isolate the more subtle roles of ocean circulation changes versus mixed layer ocean-atmosphere interactions. (Hereafter we refer to these different experiments and ocean model complexities using the notation "$Experiment_{model}$", such as "$WM_{DOM}$" for the White Mountain experiment featuring a fully dynamical ocean model.) Each of these experiments (summarized in Table 1) was integrated until the climate system (including the deep ocean for DOM simulations) reached close to radiative equilibrium (see DiNezio et al., 2018 Supplementary Materials Section S5 for more details). Each was then integrated forward at equilibrium for an additional number of years (Table 1) to calculate climatological fields for comparison.

Unless otherwise stated, all climate anomalies reported in this study are at least 95% significant using a Student's *t*-test and are relative to a CTL experiment run with the corresponding ocean model complexity. When compared to CTL, atmospheric circulation anomalies in WM are due to the combination of ice sheet albedo and topography (i.e., the combination of mechanical and thermodynamic forcing), while circulation anomalies in GM are due to mechanical forcing from the topography alone. Their difference (WM minus GM) estimates the climate response to ice sheet albedo alone (i.e., thermodynamic forcing only). Differencing WM and GM simulations to isolate the direct ice sheet albedo forcing on the climate system implicitly assumes that ice sheet mechanical and thermodynamic forcing are linearly additive. To assess the validity of this assumption, we analyze an additional albedo-forced CESM1 simulation also conducted by DiNezio et al. (2018). This extra simulation features a dynamical ocean model and was forced with the distribution of continental ice set at LGM values, but over the modern topography. All other boundary conditions (GHGs, orbital, topography, etc.) were set to pre-industrial values. This approach isolates the cooling effect of the albedo of the ice sheets relative to modern topography. Following the naming convention of our other experiments, we refer to this fully coupled simulation as White Plains ($WP_{DOM}$; Table 1 and Fig. 1). By comparing $WP_{DOM}$ anomalies to those from $WM_{DOM}$ we are able to discern whether the elevation of the ice sheet albedo forcing introduces significant nonlinearities in the large-scale climate response.

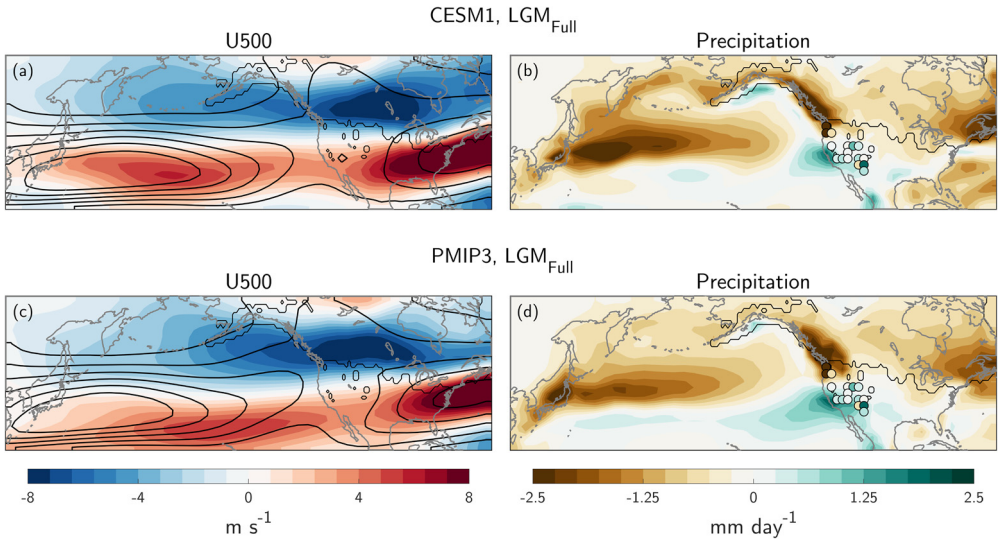


**Fig. 2.** North Pacific climate at the Last Glacial Maximum. Difference maps of $LGM_{Full}$ minus CTL (a) 500 mb zonal wind (U500; m s$^{-1}$) and (b) precipitation (mm day$^{-1}$) averaged during boreal winter (December-February). Thick black contours in (a) show wintertime U500 climatology in the pre-industrial control (contour interval is 5 m s$^{-1}$ with max value of 30 m s$^{-1}$). (c)–(d) As in (a)–(b), but for the ensemble mean of seven PMIP3 models forced with full LGM boundary conditions minus their respective pre-industrial control simulations. Thin black contour in each panel marks approximate ice sheet edge at the LGM. Filled circles in (b) and (d) show precipitation changes from proxy estimates (Table S2).

Finally, to test the sensitivity of our $LGM_{Full}$ results to our choice of model, we compare $LGM_{Full}$ to an ensemble of seven models forced with identical LGM boundary conditions taken from the PMIP3 archive. These models are listed in Table S1.

### 2.2. Precipitation and sea surface temperature proxy estimates

We validate our simulated hydroclimate results against several proxy estimates of LGM western North American precipitation change, as in Lora et al. (2017). These proxies consist primarily of pollen data (Bartlein et al., 2011), but also include other quantitative precipitation estimates (Ibarra et al., 2014; Lemons et al., 1996; Maher et al., 2014; Thompson et al., 1999). In addition, we compare simulated North Pacific SST anomalies to the gridded proxy estimates generated by Tierney et al. (2020). These estimates combine a large collection of geochemical proxies of SST with an isotope-enabled version of CESM to produce a spatially coherent reconstruction of LGM temperatures using data assimilation. Specifically, we use version 2.0 of their LGM data assimilation runs, which features a wider array of model priors than the original dataset. See Tierney et al. (2020) for more details.

## 3. Results

Our CESM1 $LGM_{Full}$ experiment produces patterns of North Pacific atmospheric circulation and North American west coast hydroclimate change that compare well with the ensemble mean results of seven PMIP3 models forced with the same LGM boundary conditions (Fig. 2). Specifically, both our CESM1 $LGM_{Full}$ simulation and the PMIP3 models produce a clear north-south dipole in boreal winter precipitation anomalies along the North American west coast (Fig. 2b, d), such that the Southwestern U.S. is wetter than modern and the Pacific Northwest, from Washington to Alaska, is drier than modern. These similarities are further highlighted by the spatial pattern correlation between our CESM1 $LGM_{Full}$ simulation and the PMIP3 ensemble mean, which is $R = 0.92$ for the zonal wind anomalies and $R = 0.85$ for the precipitation change, both significant at 95% confidence.

The simulated precipitation anomalies are also highly correlated in space with the proxy reconstructions of LGM-to-present precipitation changes (circles Fig. 2b, d and Table S2). The correlation between the proxy estimates and the $LGM_{Full}$ precipitation anomalies at the nearest grid cell is $R = 0.67$, which is significant at 95% confidence. These precipitation changes are due to an intensified and southward shifted wintertime jet stream, which correspondingly shifts southward the distribution of landfalling North Pacific storms (Fig. 2a, c). These model-data comparisons are consistent with many previous studies (Anderson et al., 1988; Bartlein et al., 2011; Ibarra et al., 2014; Lachniet et al., 2014; Lemons et al., 1996; Lora, 2018; Lora et al., 2017; Maher et al., 2014; Oster et al., 2015; Owen et al., 2003; Seltzer et al., 2019; Thompson et al., 1999) and give us confidence in our CESM1 modeling framework.

### 3.1. North Pacific climate response to ice sheet topography

Direct orographic forcing from the ~3 km (Fig. 1b) tall North American ice sheets in $GM_{AGCM}$ produces a southward displacement and intensification of the wintertime North Pacific jet, as well as a general tendency for a north-south shift in west coast hydroclimate (Fig. 3a–b), which is similar to the coupled response with full LGM forcings (Fig. 2a–b). In particular, $GM_{AGCM}$ produces a strong deceleration of the westerlies at ~50°N (Fig. 4a) and throughout the atmospheric column that closely aligns with the latitude at which LGM North American ice sheets begin to rise above modern topography (Fig. 4a; orange and purple lines), indicative of a direct mechanical slowdown of the westerly flow ahead of the elevated land surface at these latitudes. The weakened atmospheric circulation is then steered southward, leading to an acceleration of the westerlies near 30°N. Overall, these zonal wind anomalies produce an equatorward shift of the North Pacific jet stream, especially in the mid-to-lower troposphere. These circulation changes are apparent in the boreal winter geostrophic streamfunction (Fig. S1a), which shows an anomalous low over the North Pacific as part of a generally barotropic stationary wave response throughout the Northern Hemisphere, consistent with results presented by Roberts et al. (2019) using a different climate model.

Based on the similarities between $GM_{AGCM}$ (Fig. 3a–b) and $LGM_{Full}$ (Fig. 2a–b), one might reach the same conclusion as many prior AGCM-based studies that also sought to disentangle the role of ice sheet topography versus ice sheet albedo on LGM climate (Anderson et al., 1988; Bartlein et al., 1998; Bromwich et al., 2004;

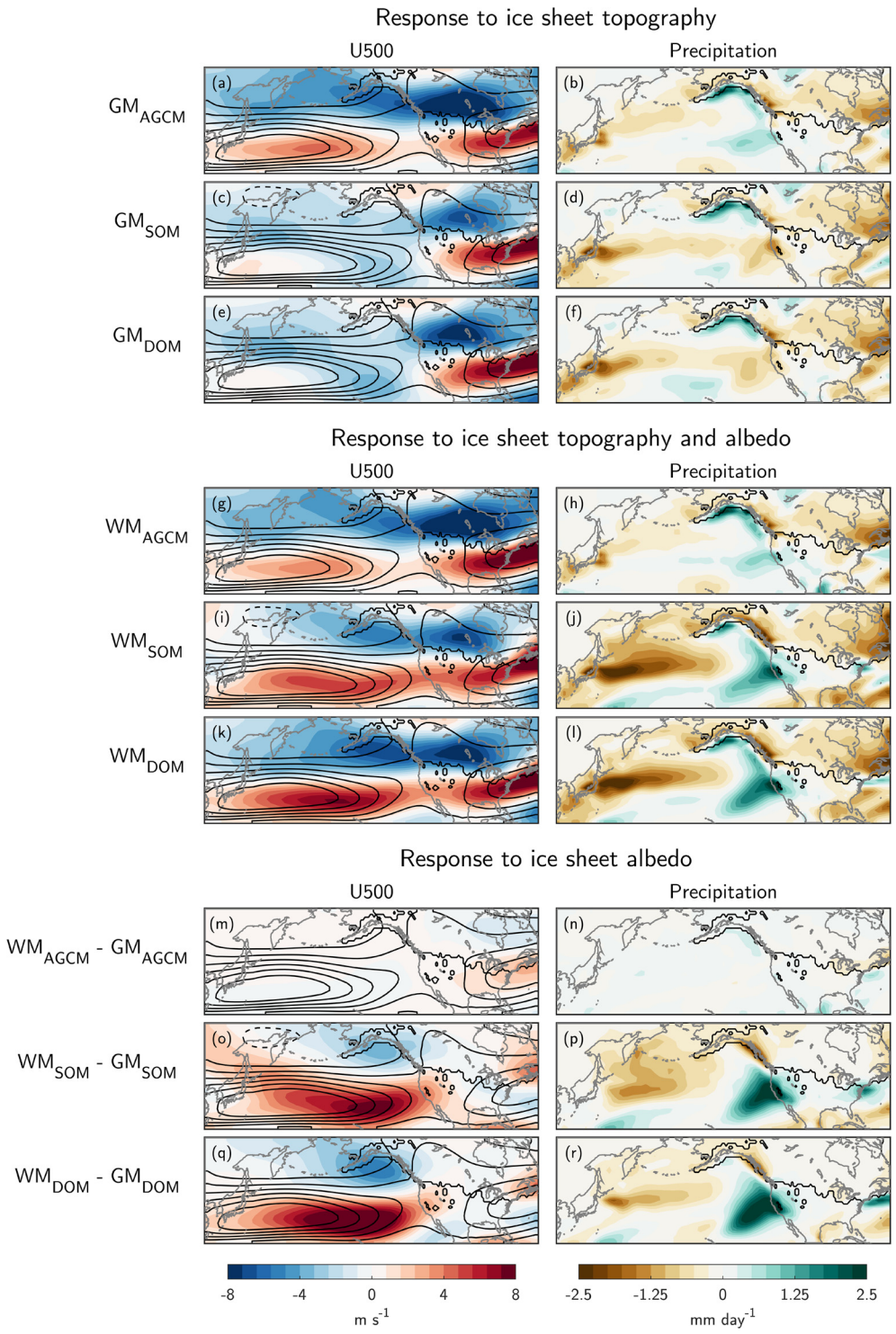


**Fig. 3.** North Pacific boreal winter response of 500 mb zonal wind (U500) and precipitation in single forcing experiments: (a)–(f) GM–CTL, (g)–(i) WM–CTL, and (m)–(r) WM−GM in their respective ocean configurations. Thick black contours in show wintertime U500 climatology in the pre-industrial control (contour interval is 5 $m s^{-1}$ with max value of 30 $m s^{-1}$).

Cook and Held, 1988; Kim et al., 2008; Kutzbach and Wright, 1985; Manabe and Broccoli, 1985)—that ice sheet topography alone is sufficient to explain the overall changes to the LGM North Pacific jet stream, without the need for ocean-atmosphere interactions. However, when coupling our AGCM to interactive ocean models, we in fact find nearly the opposite result. Specifically, both $GM_{SOM}$ and $GM_{DOM}$ show a broad deceleration of the westerlies without a clear latitudinal shift in the jet stream (Figs. 3c, e and 4b–c) as well as drier conditions in the Southwestern U.S. relative to the control (Fig. 3d, f). This raises a key question: What ocean-atmosphere feedbacks and/or ocean circulation changes lead to such markedly divergent circulation and hydroclimate responses between our uncoupled ($GM_{AGCM}$) and coupled ($GM_{SOM}$ and $GM_{DOM}$) simulations?

Of central importance to addressing this question is the SST warming observed throughout much of the subpolar North Pacific in $GM_{DOM}$ (Fig. 5d) and $GM_{SOM}$ (Fig. S2a). These warm anomalies

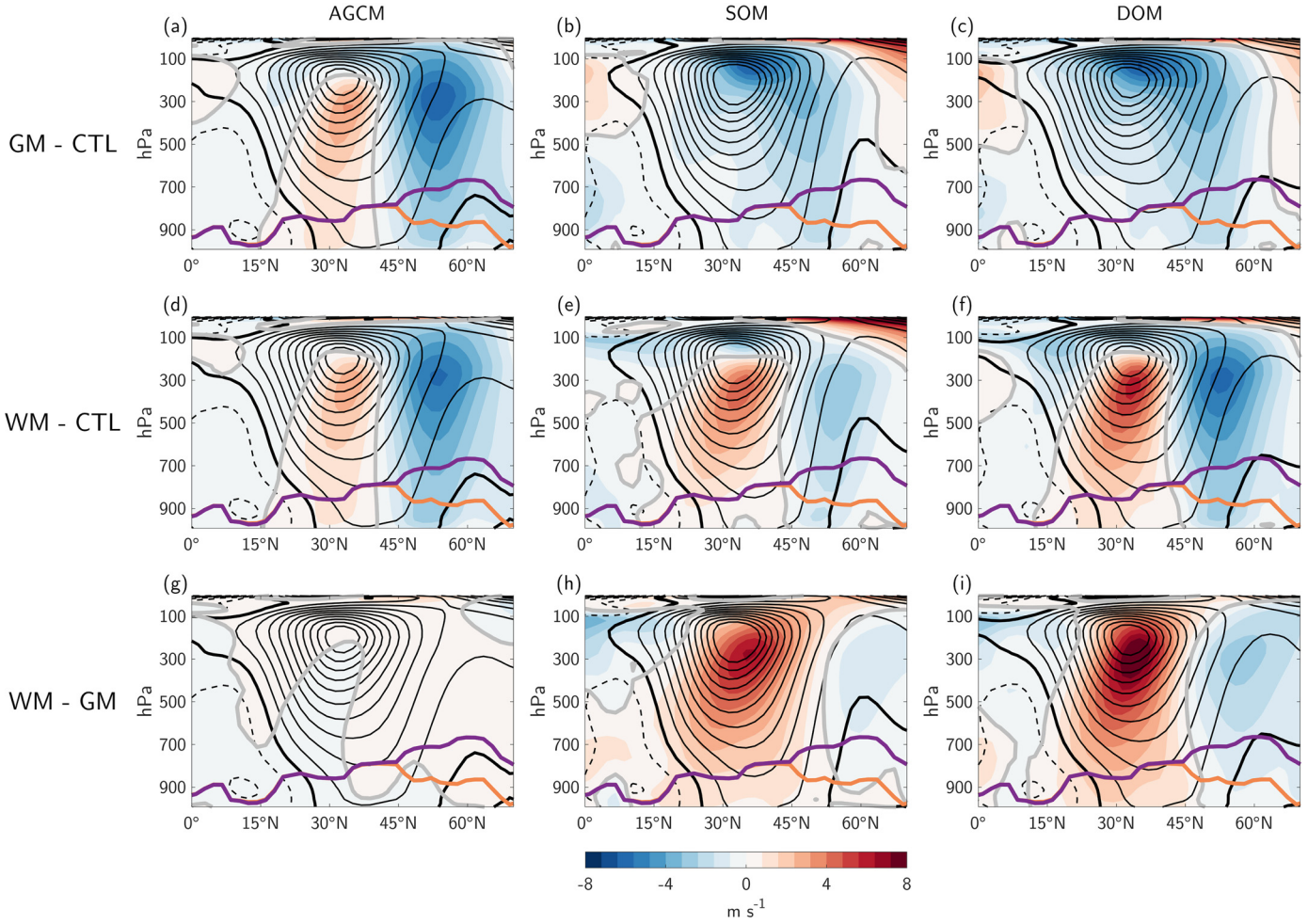


**Fig. 4.** North Pacific zonal wind response. Latitude-height cross-sections of boreal winter (December-February) zonal wind anomalies (shading; $m\,s^{-1}$) zonally averaged over the Pacific basin (120°E-110°W). Anomalies are for (a)–(c) GM minus CTL, (d)–(f) WM minus CTL, and (g)–(i) WM minus GM in their respective (left column) AGCM, (middle column) SOM, and (right column) DOM ocean configurations. Purple and orange contours roughly outline the profile of North American topography at each latitude (i.e., as if looking westward from the Atlantic Ocean) for LGM and CTL, respectively. Black contours denote the winter CTL zonal wind climatology for this region. Solid (dashed) black contours denote positive (negative) values. Black contour interval is 5 $m\,s^{-1}$ starting at 0 $m\,s^{-1}$ (thick black contour). Thick gray contour marks the 0 $m\,s^{-1}$ zonal wind anomaly contour.

extend upward throughout the atmospheric column (Fig. S3b-c), decreasing the meridional temperature gradient between the tropics and the poles, and weakening the North Pacific jet stream by thermal wind balance. An ocean mixed layer heat budget (Supplementary Materials Section S1; Fig. S4) indicates that this anomalous subpolar warming can be attributed primarily to three important factors: (1) increased surface shortwave radiation due to decreased low clouds, (2) decreased evaporative cooling driven by the mechanically weakened surface westerlies, and (3) a dynamical ocean response that primarily reflects warm SST advection via Ekman transport (Fig. S6a–b). In contrast, without the added atmospheric response to anomalous ocean temperatures, $GM_{AGCM}$ produces cool anomalies in the mid-troposphere near ~40°N (Fig. S3a), consistent with cold air advection from high-latitudes by the anomalous low (Fig. S1a). This cooling enhances the local meridional temperature gradient and reinforces the direct mechanical shift of the jet stream, opposite to the behavior observed in $GM_{SOM}$ and $GM_{DOM}$.

The subpolar warming seen in $GM_{DOM}$ is a robust response to ice sheet mechanical forcing, even when considering the additional impacts of lower LGM GHGs (see Supplementary Materials Section S2). This is because reducing GHGs does not significantly alter the anomalous meridional temperature gradient set up by the direct mechanical ice sheet forcing in $GM_{DOM}$. However, adding in the full range of altered LGM boundary conditions (including ice sheet albedo) does lead to a much different SST response than in $GM_{DOM}$. In particular, $LGM_{Full}$ exhibits colder-than-modern conditions throughout the North Pacific (Fig. 5c), with the coldest SST anomalies found near the Kuroshio Extension region in a pattern that broadly resembles a positive phase of the Pacific Decadal Oscillation (PDO; Mantua et al., 1997).

This PDO-like cooling is supported by various proxy reconstructions of North Pacific SSTs (Fig. 5a) (Gray et al., 2020; Rae et al., 2020; Tao et al., 2013; Tierney et al., 2020), and is also seen in the PMIP3 models analyzed here (Fig. 5b and Fig. S8) as well as more recent PMIP4-era models (Kageyama et al., 2021). We do note that, while both our $LGM_{Full}$ simulation and the PMIP3 ensemble mean show weak cooling in the subpolar North Pacific, proxy estimates indicate that the subpolar LGM may have been slightly warmer than modern (Rae et al., 2020). Although, these warm anomalies may have been largely confined to a relatively small area north of 50°N (Fig. 5a). Regardless, the broad-scale differences between the ice sheet-driven SST anomalies in our $GM_{DOM}$ and $LGM_{Full}$ experiments further suggest that ocean adjustment to direct mechanical ice sheet forcing (i.e., extensive subpolar North Pacific warming) is not a foundational component of the overall response of the coupled climate system to full LGM boundary conditions.

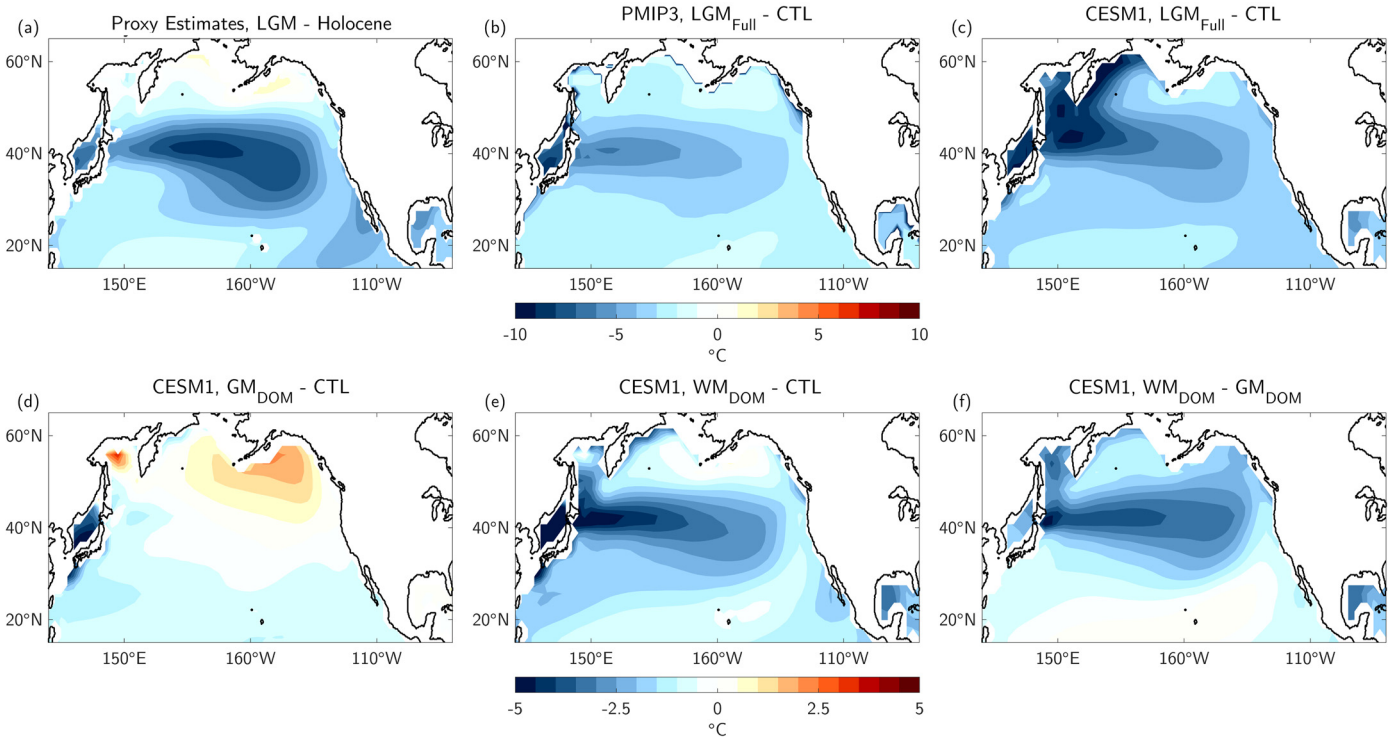


**Fig. 5.** Simulated ocean temperature response. Difference maps of annual mean SSTs (°C) in (a) LGM minus late Holocene data assimilated proxy estimates from Tierney et al. (2020), (b) the ensemble mean of seven PMIP3 models forced with full LGM boundary conditions minus their respective pre-industrial control simulations, (c) CESM1 $LGM_{Full}$ minus CTL, (d) CESM1 $GM_{DOM}$ minus CTL, (e) CESM1 $WM_{DOM}$ minus CTL, and (f) CESM1 $WM_{DOM}$ minus $GM_{DOM}$.

### 3.2. North Pacific climate response to ice sheet albedo

We now consider the combined contributions of elevated ice sheet topography (as in GM) and high ice sheet surface albedo to the overall LGM North Pacific climate response. In $WM_{AGCM}$, the zonal wind and precipitation anomalies are very similar to $GM_{AGCM}$ (Figs. 3a–b and 3g–h). Differencing the $WM_{AGCM}$ and $GM_{AGCM}$ simulations, we see little response in the zonal wind and precipitation, thus ice sheet topography is almost entirely responsible for the large-scale atmospheric response in both of these uncoupled simulations (Figs. 3m-n). This result is consistent with Roberts et al. (2019), who showed that the wintertime North Pacific stationary wave response to ice sheet topography is similar to the response to ice sheet topography and ice sheet albedo combined (see their Fig. 2). Indeed, our $WM_{AGCM}$ and $GM_{AGCM}$ simulations produce nearly identical wintertime stationary wave fields to theirs (Figs. S1a and S1g). When coupled to an ocean model in $WM_{SOM}$ and $WM_{DOM}$, the additional thermodynamic forcing from high ice sheet albedo is responsible for an intensification and southward displacement of the boreal winter North Pacific jet, particularly in the central/eastern North Pacific, leading to the characteristic north-south dipole in western North American precipitation (Fig. 3i–l). This can be seen more clearly when differencing the respective WM and GM simulations (Fig. 3o–r).

To what extent can the differences between our WM and GM simulations be explained by ice sheet albedo versus potential nonlinearities in the climate system? Our $WP_{DOM}$ simulation isolates the climate response to ice sheet albedo relative to modern day topography, and provides a useful tool to address this question. In $WP_{DOM}$, the boreal winter North Pacific jet experiences an intensification and southward shift that is qualitatively similar to that seen in $WM_{DOM}$ minus $GM_{DOM}$ (Fig. S9a, c). This leads to a north-south shift in precipitation in $WP_{DOM}$ that is also comparable to $WM_{DOM}$ minus $GM_{DOM}$ (Fig. S9b, d). Similar results are seen when comparing anomalies from $WM_{DOM}$ to the linear combination of anomalies from $WP_{DOM}$ and $GM_{DOM}$ (Fig. S9e–h). While the spatial patterns of anomalies between the different ice sheet albedo forcing estimates are qualitatively similar, the zonal wind anomalies in $WP_{DOM}$ tend to be weaker than in $WM_{DOM}$ and the moistening signal in the southwest U.S. is overall less clear in $WP_{DOM}$. These results suggest that some nonlinearities likely contribute to the differences between our WM and GM simulations and that WM minus GM should not be quantitatively interpreted. Instead, the albedo forcing estimates provided by taking WM minus GM (i.e., Figs. 3m–r and 4g–i) should be seen as a qualitative indicator of how elevated ice sheet albedo forcing imprints on large-scale climate.

The $WP_{DOM}$ experiment discussed above is an idealized representation of LGM conditions (i.e., it is unlikely that there would ever be such extensive ice sheet albedo forcing across relatively low topography in the real world). However, our $WM_{DOM}$ simulation provides a much more realistic representation of total ice sheet forcing with which to compare to our full LGM simulation. For example, the $WM_{SOM}$ and $WM_{DOM}$ zonal wind and precipitation anomalies are nearly identical to those seen in $LGM_{Full}$ (comparing Figs. 2a–b and 3i–l), suggesting that thermodynamic forcing from the bright ice sheets is key in setting the overall LGM North Pacific atmospheric response. However, these anomalies are also heavily reliant upon coupled ocean-atmosphere interactions, as indicated by the difference of WM minus GM zonal wind fields across the different ocean configurations (Fig. 3m–r and Fig. 4g–i). In particular, ocean-atmosphere coupling enables an albedo-forced acceleration of the westerlies throughout the atmospheric column between ~30–40°N in $WM_{SOM}$ and $WM_{DOM}$. This response is only slightly larger in $WM_{DOM}$, indicating that dynamical ocean circulation changes are of secondary importance to mixed layer air-sea interactions in driving these anomalies. Overall, our experiments suggest that the inclusion of ocean-atmosphere coupling in $WM_{SOM}$ and $WM_{DOM}$ acts to reinforce the mechanically induced southward jet shift implied by the uncoupled $WM_{AGCM}$ (Fig. 4g).

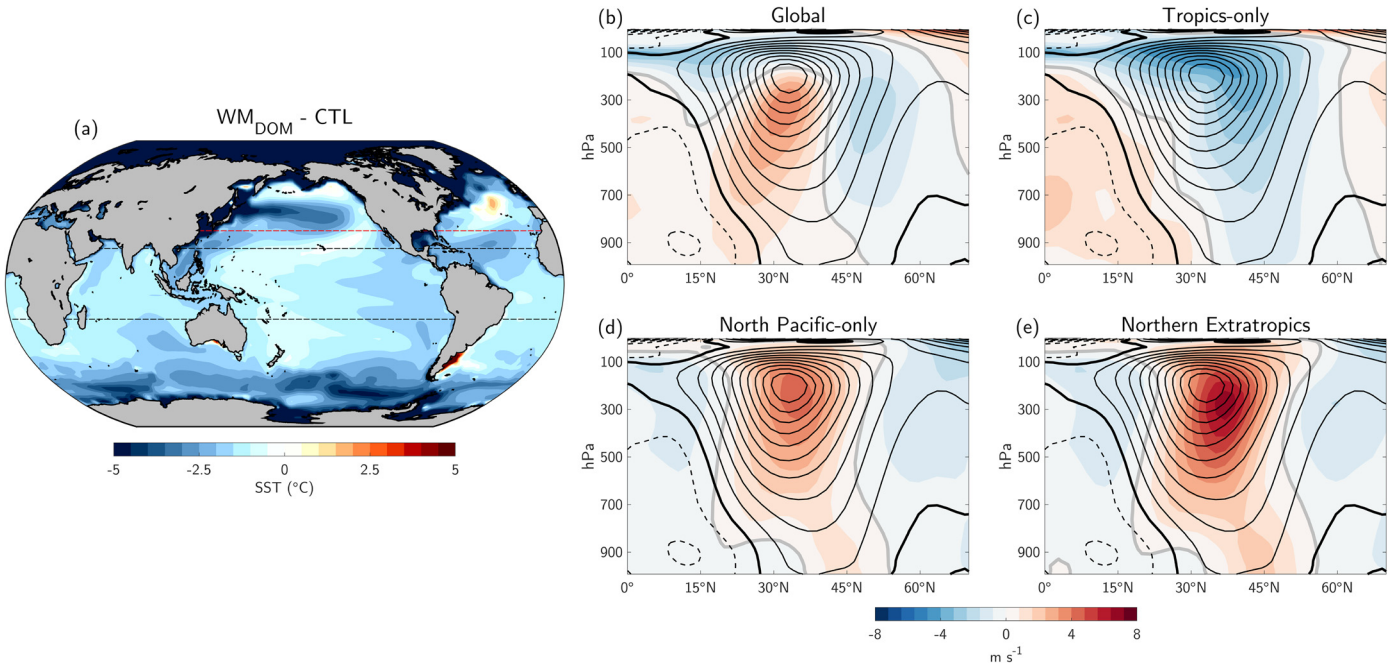


**Fig. 6.** North Pacific zonal wind response in WM$_{SST}$. (a) Global SST anomalies (°C) for WM$_{DOM}$ minus CTL averaged during December-February. (b)–(e) Latitude-height cross-section of boreal winter (December-February) zonal wind anomalies (shading; m s$^{-1}$) zonally averaged over the Pacific basin (120°E-110°W). Anomalies are from the WM$_{SST}$ CAM5 simulations forced with WM$_{DOM}$ SSTs (b) globally, (c) in the tropics-only (20°S–20°N; equatorward of dashed black lines), (d) in the North Pacific-only (>30°N; poleward of red dashed line in North Pacific), and (e) in the Northern Hemisphere extratropics (>30°N; poleward of the red dashed line at all longitudes). Black contours in (b)–(e) denote the winter WM$_{SST}$ control zonal wind climatology for this region. Solid (dashed) black contours denote positive (negative) values. Black contour interval is 5 m s$^{-1}$, with the thick black contour marking 0 m s$^{-1}$. Thick gray contour marks the 0 m s$^{-1}$ zonal wind anomaly contour.

How do ocean-atmosphere feedbacks and/or ocean circulation changes combine with the direct atmospheric response to thermodynamic ice sheet forcing to form the wintertime WM$_{SOM}$ and WM$_{DOM}$ North Pacific climate anomalies? Both WM$_{DOM}$ (Fig. 5e) and WM$_{SOM}$ (Fig. S2b) produce PDO-like SST anomaly patterns that are similar to that seen in proxy estimates, our CESM1 LGM$_{Full}$, and the PMIP3 ensemble mean (Fig. 5a–c). However, the peak anomalies in WM$_{DOM}$—exceeding −4 °C in magnitude—are only about half as large as in LGM$_{Full}$ since the latter experiences additional cooling from changes in orbital configuration and lower GHGs.

Using a mixed layer heat budget analysis, we find that the WM$_{DOM}$ cooling primarily results from: (1) decreases in downward surface shortwave radiation south of 40°N, (2) ocean circulation changes poleward of 40°N, and (3) increased evaporation from strengthened surface winds and an increased air-sea temperature contrast (Fig. S5). The cooling generated by ocean circulation changes has contributions from anomalous Ekman heat advection (Fig. S6c–d), but is also consistent with a southward expansion of the North Pacific subpolar gyre circulation and a southward shift of the subarctic SST front in response to strengthened polar easterlies (Gray et al., 2020). The anomalous temperatures around 40°N extend throughout much of the atmospheric column to ∼300 mb, increasing the meridional temperature gradient over the North Pacific and strengthening the jet stream in WM$_{SOM}$ and WM$_{DOM}$ by thermal wind balance (Fig. S3e–f).

To confirm that the underlying SST field is indeed driving the boreal winter upper-level zonal wind response, we conducted an additional set of AGCM simulations forced with pre-industrial land surfaces (i.e., no LGM ice sheets) and the long-term monthly mean SST output from WM$_{DOM}$ (referred to as WM$_{SST}$; see Supplementary Materials Section S3). The consistency between the WM$_{SST}$ global experiment and WM$_{DOM}$ is striking (Figs. 4f and 6b), and suggests that nearly the entire LGM North Pacific atmospheric circulation—and thus North American hydroclimatic—response during boreal winter is attributable to the ice sheet-driven SST field and not to the direct atmospheric response to the combined effects of ice sheet orography and albedo (as estimated by WM$_{AGCM}$). Regional SST forced experiments show that the aforementioned North Pacific SST pattern accounts for the majority of the global SST forced response, particularly the accelerated westerlies between ∼30°–40°N (Fig. 6c–e). Therefore, the direct atmospheric response to continental ice sheets is only important to the extent that it contributes to the formation of this PDO-like SST pattern (Fig. 5e).

### 3.3. *Physical mechanisms linking ice sheet albedo to North Pacific SST changes*

The North Pacific ocean and atmosphere are highly coupled in boreal winter (Alexander, 1992; Alexander and Scott, 1997). Therefore, it is important to diagnose the extent to which the SST cooling described above is a source or a symptom of the atmospheric circulation anomalies in the WM experiments. In doing so, we can better understand the physical pathways by which the direct large-scale atmospheric response to a tall/bright ice sheet (as in WM$_{AGCM}$) first imprints onto the North Pacific ocean before coupling back to the atmosphere (as in WM$_{SOM}$/WM$_{DOM}$). The direct thermodynamic impact of North American ice sheets on the large-scale atmosphere should be strongest in boreal summer when the zonal winds are weakest and most sensitive to diabatic heating (Roberts et al., 2019; Ting, 1994). Additionally, anomalous cooling over land caused by high ice sheet albedo will be largest in summer when there is more insolation to reflect.

The seasonally varying influence of ice sheet albedo on large-scale atmospheric circulation was discussed in detail by Roberts et al. (2019), and is reproduced here as the difference between WM and GM stationary wave fields in our AGCM simulations (Fig. S1m–r). Importantly, the summertime atmospheric circulation anomalies are more similar across the AGCM/SOM/DOM configurations than those in winter for both WM and GM simulations. The insensitivity of the boreal summer climate response to the presence of an

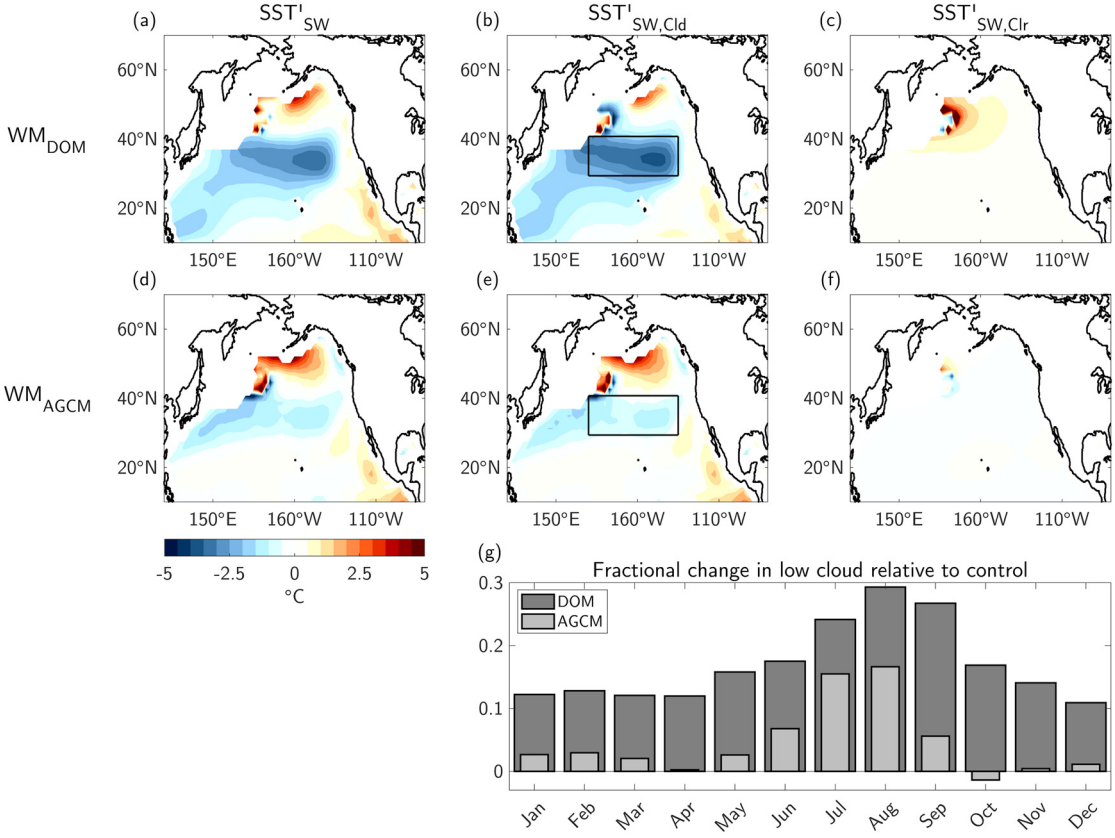


**Fig. 7.** Impact of clouds on ocean temperatures. SST anomalies implied by changes in annual mean (a) net surface shortwave, (b) shortwave cloud radiative forcing, and (c) clear-sky surface shortwave in $WM_{DOM}$. (d)–(f) Same as (a)–(c), but for $WM_{AGCM}$. (g) Monthly fractional change (relative to CTL) in low cloud amount, averaged in black boxes in (b) and (e) for $WM_{DOM}$ (dark gray) and $WM_{AGCM}$ (light gray).

ocean in our simulations suggests that the ocean and the large-scale atmosphere are largely decoupled during this season. This is confirmed in our additional $WM_{SST}$ experiment, which does not reproduce the $WM_{DOM}$ zonal wind anomalies in boreal summer (not shown). Therefore, by relating the WM annual mean SST cooling (Fig. 5e) to summer North Pacific climate anomalies, we can reliably diagnose the direct atmospheric response to the tall/bright ice sheet, even in our coupled simulations.

As discussed previously, decreases in surface shortwave radiation play an integral role in cooling the North Pacific in $WM_{DOM}$, with cloud changes accounting for nearly the entire surface shortwave contribution to the SST anomalies (Fig. 7a–c). Our simulation shows an increase in total cloud fraction in this region; however, the shortwave cloud radiative forcing (Fig. 7b) is primarily due to an increase in low clouds, such as marine stratocumulus (Fig. 8a). Low-lying marine stratocumulus clouds are an important amplifying factor for SST anomalies in the North Pacific (Norris et al., 1998; Ronca and Battisti, 1997), often producing a positive feedback with increasing (decreasing) SSTs leading to decreasing (increasing) low cloud amounts and consequently more (less) downward shortwave radiation at the surface (Amaya et al., 2020).

Direct ice sheet-driven large-scale atmospheric circulation changes can be connected to local SST anomalies independent of these ocean-atmosphere feedbacks in $WM_{AGCM}$. This uncoupled simulation produces a strikingly similar pattern of surface shortwave-induced SST anomalies, which are also dominated by changes in shortwave cloud radiative forcing (Fig. 7d–f). Aside from the similar spatial pattern, the anomalies are generally weaker in $WM_{AGCM}$ than in $WM_{DOM}$, suggesting that local low cloud-SST feedback amplifies both the low cloud and SST response in $WM_{DOM}$. Averaging the fractional change in low cloud amount in the central North Pacific, we see that the increase in low clouds in $WM_{AGCM}$ and $WM_{DOM}$ is largest in boreal summer (Fig. 7g), with the difference between the two further highlighting the role of ocean-atmosphere feedbacks in amplifying these changes in $WM_{DOM}$ throughout the year.

The increase in summertime low cloud coverage in both $WM_{AGCM}$ and $WM_{DOM}$ is due primarily to a stronger temperature inversion above the marine boundary layer west of ~160°W and increased moisture east of ~160°W (Fig. 8). These changes are driven by an anomalous cyclonic circulation in the lower atmosphere seen in each of our WM simulations during boreal summer (Fig. S1j–l). This low pressure anomaly advects cold air from the high latitudes in the western North Pacific (increasing stability at low levels), while advecting additional moisture from the tropics in the eastern North Pacific. See Supplementary Materials Section S1.2 for more details on the cloud parameters analyzed here.

Overall, the consistent change in cloudiness in the $WM_{AGCM}$ simulation provides evidence that the direct large-scale atmospheric response to North American ice sheets first influences North Pacific SSTs during boreal summer through changes in cloud fraction and surface shortwave radiation. These SST anomalies then persist into winter through a combination of positive feedbacks including low cloud-SST and wind-evaporation-SST interactions, as well as ocean circulation adjustments, where they then strongly influence the position of the North Pacific jet and, by extension, North American west coast hydroclimate.

## 4. Summary

In this study, we investigated the influence of continental ice sheets on North Pacific atmospheric circulation and North American west coast hydroclimate during the LGM. Our model results showed that, in response to full LGM boundary conditions (e.g.,

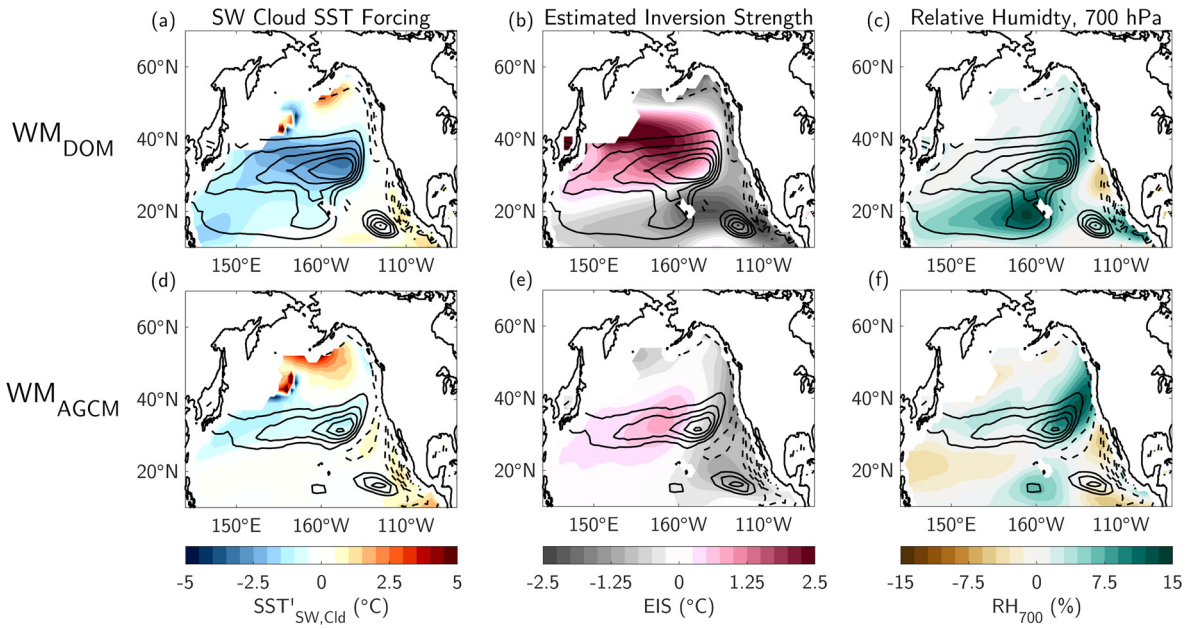


**Fig. 8.** Low cloud controlling factors. (left column) SST anomalies implied by changes in annual mean shortwave cloud radiative forcing (shading; °C), (middle column) Estimated Inversion Strength (EIS; shading; °C) anomalies averaged during boreal summer (June-August), and (right column) relative humidity anomalies (shading; %) at 700 mb averaged during boreal summer in (a)–(c) $WM_{DOM}$ minus CTL and (d)–(f) $WM_{AGCM}$ minus CTL. Black contours in each panel depict the corresponding change in summertime averaged low cloud fraction (e.g., $WM_{DOM}$ minus CTL over CTL). Solid (dashed) black contours denote positive (negative) values. Contour interval is 0.1 starting at 0.1. See Supplementary Materials Section S1.2 for more details on the cloud parameters analyzed here.

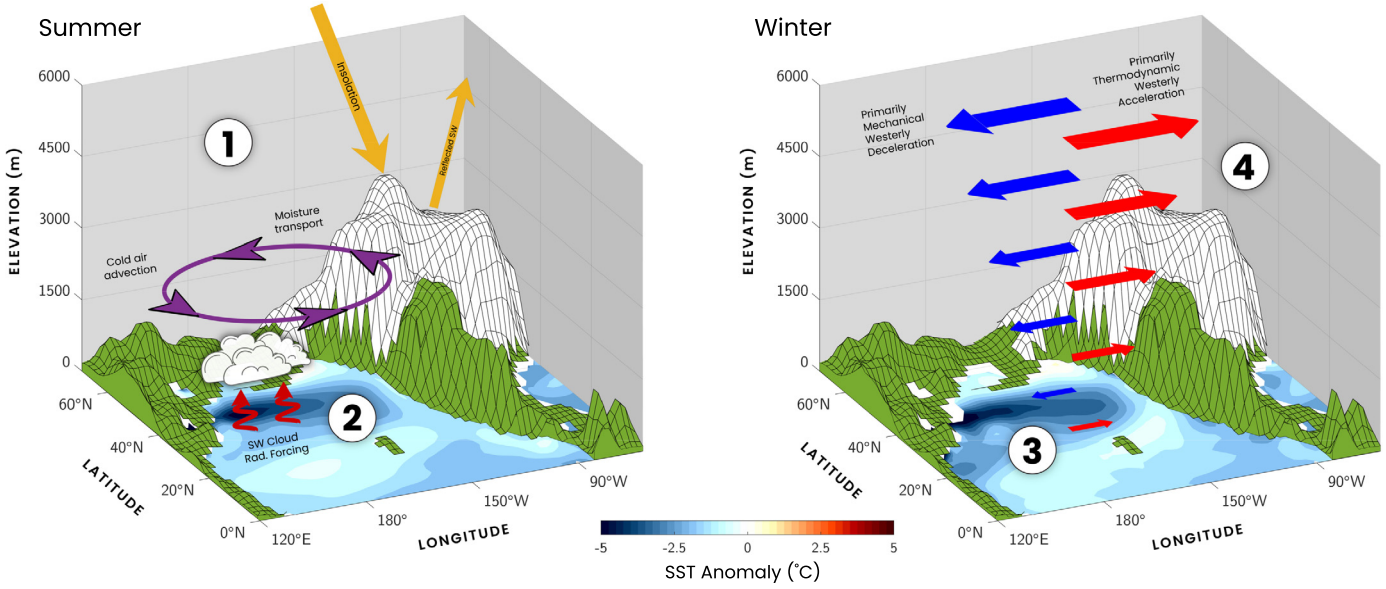


**Fig. 9.** Schematic summary of the North Pacific coupled climate response to tall/bright North American ice sheets during the LGM. (1) A direct stationary wave response to the tall/bright ice sheets during boreal summer produces a low-level cyclonic circulation over the North Pacific. These circulation anomalies drive cold air advection in the western North Pacific and increased water vapor transport in the eastern North Pacific. (2) Enhanced stability coupled with increased atmospheric moisture leads to more marine stratocumulus clouds, which reflect sunlight and cool the North Pacific Ocean near ~40°N. (3) Low cloud-SST feedback and ocean dynamical adjustments amplify the SST and cloud changes, persisting them into boreal winter. (4) The enhanced North Pacific meridional temperature gradient accelerates the westerlies on the equatorward flank of the jet stream, while mechanical interactions with ice sheet topography decelerate the flow on the poleward flank. Overall, this leads to a southward shift of the North Pacific jet stream and a redistribution of North American west coast hydroclimate during the LGM.

GHGs, ice sheets, sea level, orbital configuration, etc.), the North Pacific jet is intensified and shifted southward during boreal winter. This results in a wetter-than-modern-day Southwest U.S. and a drier-than-modern-day Pacific Northwest, consistent with previous model simulations and paleoproxy reconstructions (Anderson et al., 1988; Bartlein et al., 2011; Benson et al., 2011; Ibarra et al., 2014; Kirby et al., 2013; Lachniet et al., 2014; Lemons et al., 1996; Lora et al., 2017; Maher et al., 2014; Oster et al., 2015; Owen et al., 2003; Reheis et al., 2012; Seltzer et al., 2019; Thompson et al., 1999). Decomposing this climate response into contributions from ice sheet topography alone (i.e., Green Mountain) and ice sheet topography plus albedo (i.e., White Mountain), we found that these circulation changes result from a complex combination of mechanical and thermodynamic ice sheet effects that are critically dependent on the presence of ocean-atmosphere interactions.

The step-by-step response of the North Pacific atmosphere to realistic continental ice sheets (i.e., a White Mountain) is summarized in the schematic Fig. 9. In short, the large-scale stationary

wave response to tall/bright ice sheets includes a low-level cyclonic circulation over the North Pacific during boreal summer, supported also by previous studies (Roberts et al., 2019). This circulation anomaly increases moisture transport to the eastern North Pacific, while simultaneously advecting cool air from high-latitudes over the western North Pacific. The increase in moisture combined with the increased lower atmosphere stability leads to an increase in low clouds, which cool North Pacific SSTs between 30°N-40°N by reducing downward surface shortwave radiation. A positive low cloud-SST feedback and subpolar gyre dynamical adjustments (Gray et al., 2020) then combine to amplify both the cloud changes and the North Pacific SST anomalies, allowing them to persist into boreal winter. During the winter, the ocean couples back to the large-scale atmosphere and reinforces the tendency for a topographically-forced southward shift of the North Pacific jet stream by increasing the North Pacific meridional temperature gradient and accelerating the westerlies on the equatorward flank of the jet.

## 5. Discussion

Many of the above results are consistent with previous studies (e.g., Roberts et al., 2019; Yanase and Abe-Ouchi, 2010), who used similar model simulations to investigate the importance of different ice sheet characteristics to LGM atmospheric circulation as well as the influence of ocean coupling in shaping those responses. However, our detailed analysis of North Pacific SST patterns helps to fill a notable gap in our understanding of the specific physical pathways (e.g., low cloud feedbacks) by which the coupled climate system adjusts to LGM ice sheet forcing, and helps to further highlight the relevance of LGM climate for modern applications. In particular, our finding that ice sheet-driven SST patterns—rather than the direct atmospheric response to mechanical forcing induced by the elevated topography of the LGM ice sheets—drove much of the North Pacific atmospheric circulation response during the LGM has key implications for present day climate variability and future change.

We suggest that the primary role of ice sheets on LGM hydroclimate was to provide a suitably large perturbation to the climate system that led to the formation of an SST pattern that bears strong resemblance to a well-known climatic mode (e.g., the PDO). In this sense, while the presence (or removal) of a ~3 km tall ice sheet over North America bears no direct relevance to modern climate, the possible emergence of North Pacific SST anomalies that are similar in pattern and magnitude as those observed in our LGM simulations is distinctly plausible. While such patterns may result from natural climate variations, our findings call attention to ongoing anthropogenic factors—such as changes in Southeast Asian aerosol emissions—that have been shown to promote a PDO-like SST response in coupled models (Smith et al., 2016) and may exert a strong influence on western North American hydroclimate through air-sea interactions. These regional SST patterns may further serve to alter the expected response of the mid-latitude jet streams to future global warming (Lu et al., 2008), due to the modification of the local meridional temperature gradient at the surface.

Finally, we acknowledge several important caveats and possible sensitives regarding our analysis. For example, we note that our analysis is primarily based on simulations from a single model—CESM1.2. However, portions of our results (particularly the large-scale atmospheric circulation changes associated with different ice sheet characteristics) are nearly identical to Roberts et al. (2019), who conducted similar White Mountain and Green Mountain experiments using a different climate model. Indeed, the North Pacific stationary wave patterns in our simulations (Fig. S1) compare very well to those seen in their simulations (see Roberts et al., 2019, Figs. 2 and 3). Therefore, we have confidence that the ice sheet-driven atmospheric circulation changes discussed here are qualitatively insensitive to model choice.

Additionally, although we have identified a series of physically consistent pathways by which the coupled climate system adjusts to ice sheet forcing (Fig. 9), we note that these mechanisms depend on an accurate representation of marine stratocumulus clouds and their feedbacks. While the simulation of marine stratocumulus clouds has improved in recent model generations (Engström et al., 2014), there is still large uncertainty among models in the expected response of clouds to future greenhouse gas increase (Qu et al., 2014; Webb et al., 2013). Nevertheless, Xiao et al. (2014) showed that CESM1 credibly reproduces the climate conditions necessary to accurately simulate marine stratocumulus clouds in the North Pacific, including the depth of the planetary boundary layer, which gives us confidence in our results. Regardless, future work is needed to further explore the physical mechanisms identified here across a range of other model configurations.

## CRediT authorship contribution statement

**Dillon J. Amaya:** Conceptualization, Formal analysis, Investigation, Methodology, Project administration, Software, Supervision, Validation, Visualization, Writing – original draft, Writing – review & editing. **Alan M. Seltzer:** Conceptualization, Methodology, Writing – original draft, Writing – review & editing. **Kristopher B. Karnauskas:** Conceptualization, Methodology, Supervision, Writing – review & editing. **Juan M. Lora:** Conceptualization, Methodology, Writing – review & editing. **Xiyue Zhang:** Data curation, Methodology, Resources, Writing – review & editing. **Pedro N. DiNezio:** Data curation, Methodology, Resources, Writing – review & editing.

## Declaration of competing interest

The authors declare that they have no known competing financial interests or personal relationships that could have appeared to influence the work reported in this paper.

## Acknowledgements

We thank Shang-Ping Xie and Clara Deser for their helpful comments and suggestions during the course of this study. We also thank Simmi Sinha for her assistance in designing Fig. 9. We would like to acknowledge high-performance computing support from Cheyenne (https://doi.org/10.5065/D6RX99HX) provided by NCAR's Computational and Information Systems Laboratory, sponsored by the NSF. D.J.A. is funded by a Postdoctoral Fellowship with the Cooperative Institute for Research in Environmental Sciences (CIRES) at the University of Colorado Boulder. P.N.D. was supported by NSF (AGS 2002528). A.M.S. was funded by NSF (OCE-1923915). This work was also supported by NSF (EAR 2102984). The PMIP3 data listed in Table S2 are available at https://esgf-node.llnl.gov/projects/esgf-llnl/. The proxy precipitation data and associated uncertainties are available in Table S2. The data assimilated SST proxy estimates are from Tierney et al. (2020) and are available at https://github.com/jesstierney/lgmDA. The CESM1 simulations originally developed by DiNezio et al. (2018) and analyzed here are available at https://doi.org/10.5281/zenodo.4632397. The additional $WM_{SST}$ CAM5 simulations are available at https://doi.org/10.5281/zenodo.4632424. The figures and analyses were produced with MATLAB. MATLAB code used to perform this analysis is available from the corresponding author upon request. All data needed to evaluate the conclusions in the paper are present in the Supporting Information or at the data repositories listed above. Additional data related to this paper may be requested from the authors.

## Appendix A. Supplementary material

Supplementary material related to this article can be found online at https://doi.org/10.1016/j.epsl.2021.117271.

## References

Abe-Ouchi, A., Saito, F., Kageyama, M., Braconnot, P., Harrison, S.P., Lambeck, K., Otto-Bliesner, B.L., Peltier, W.R., Tarasov, L., Peterschmitt, J.Y., Takahashi, K., 2015. Ice-sheet configuration in the CMIP5/PMIP3 Last Glacial Maximum experiments. Geosci. Model Dev. 8, 3621–3637. https://doi.org/10.5194/gmd-8-3621-2015.

Alexander, M.A., 1992. Midlatitude atmosphere-ocean interaction during El Niño. Part I: the North Pacific ocean. J. Climate 5, 944–958. https://doi.org/10.1175/1520-0442(1992)005<0944:MAIDEN>2.0.CO;2.

Alexander, M.A., Scott, J.D., 1997. Surface flux variability over the North Pacific and North Atlantic oceans. J. Climate 10, 2963–2978. https://doi.org/10.1175/1520-0442(1997)010<2963:SFVOTN>2.0.CO;2.

Amaya, D.J., Miller, A.J., Xie, S.-P., Kosaka, Y., 2020. Physical drivers of the summer 2019 North Pacific marine heatwave. Nat. Commun. 11, 1903. https://doi.org/10.1038/s41467-020-15820-w.

Anderson, P.M., Barnosky, C.W., Bartlein, P.J., Behling, P.J., Brubaker, L., Cushing, E.J., Dodson, J., Dworetsky, B., Guetter, P.J., Harrison, S.P., Huntley, B., Kutzbach, J.E., Markgraf, V., Marvel, R., McGlone, M.S., Mix, A., Moar, N.T., Morley, J., Perrott, R.A., Peterson, G.M., Prell, W.L., Prentice, I.C., Ritchie, J.C., Roberts, N., Ruddiman, W.F., Salinger, M.J., Spaulding, W.G., Street-Perrott, F.A., Thompson, R.S., Wang, P.K., Webb, T., Winkler, M.G., Wright, H.E., 1988. Climatic changes of the last 18,000 years: observations and model simulations. Science 80 (241), 1043–1052. https://doi.org/10.1126/science.241.4869.1043.

Bartlein, P.J., Anderson, K.H., Anderson, P.M., Edwards, M.E., Mock, C.J., Thompson, R.S., Webb, R.S., Webb, T., Whitlock, C., 1998. Paleoclimate simulations for North America over the past 21,000 years: features of the simulated climate and comparisons with paleoenvironmental data. Quat. Sci. Rev. 17, 549–585. https://doi.org/10.1016/S0277-3791(98)00012-2.

Bartlein, P.J., Harrison, S.P., Brewer, S., Connor, S., Davis, B.A.S., Gajewski, K., Guiot, J., Harrison-Prentice, T.I., Henderson, A., Peyron, O., Prentice, I.C., Scholze, M., Seppä, H., Shuman, B., Sugita, S., Thompson, R.S., Viau, A.E., Williams, J., Wu, H., 2011. Pollen-based continental climate reconstructions at 6 and 21 ka: a global synthesis. Clim. Dyn. 37, 775–802. https://doi.org/10.1007/s00382-010-0904-1.

Benson, L.V., Lund, S.P., Smoot, J.P., Rhode, D.E., Spencer, R.J., Verosub, K.L., Louderback, L.A., Johnson, C.A., Rye, R.O., Negrini, R.M., 2011. The rise and fall of Lake Bonneville between 45 and 10.5 ka. Quat. Int. 235, 57–69. https://doi.org/10.1016/j.quaint.2010.12.014.

Bhattacharya, T., Tierney, J.E., DiNezio, P., 2017. Glacial reduction of the North American Monsoon via surface cooling and atmospheric ventilation. Geophys. Res. Lett. 44, 5113–5122. https://doi.org/10.1002/2017GL073632.

Broccoli, A.J., Manabe, S., 1987. The influence of continental ice, atmospheric $CO_2$, and land albedo on the climate of the Last Glacial Maximum. Clim. Dyn. 1, 87–99. https://doi.org/10.1007/BF01054478.

Bromwich, D.H., Toracinta, E.R., Wej, H., Oglesby, R.J., Fastook, J.L., Hughes, T.J., 2004. Polar MM5 simulations of the winter climate of the Laurentide Ice Sheet at the LGM. J. Climate 17, 3415–3433. https://doi.org/10.1175/1520-0442(2004)017<3415:PMSOTW>2.0.CO;2.

Cook, K.H., Held, I.M., 1988. Stationary waves of the Ice Age climate. J. Climate 1, 807–819. https://doi.org/10.1175/1520-0442(1988)001<0807:swotia>2.0.co;2.

DiNezio, P.N., Tierney, J.E., Otto-Bliesner, B.L., Timmermann, A., Bhattacharya, T., Rosenbloom, N., Brady, E., 2018. Glacial changes in tropical climate amplified by the Indian Ocean. Sci. Adv. 4. https://doi.org/10.1126/sciadv.aat9658.

Engström, A., Bender, F.A.M., Karlsson, J., 2014. Improved representation of marine stratocumulus cloud shortwave radiative properties in the CMIP5 climate models. J. Climate 27, 6175–6188. https://doi.org/10.1175/JCLI-D-13-00755.1.

Gray, W.R., Wills, R.C.J., Rae, J.W.B., Burke, A., Ivanovic, R.F., Roberts, W.H.G., Ferreira, D., Valdes, P.J., 2020. Wind-driven evolution of the North Pacific subpolar gyre over the Last Deglaciation. Geophys. Res. Lett. 47. https://doi.org/10.1029/2019GL086328.

Ibarra, D.E., Egger, A.E., Weaver, K.L., Harris, C.R., Maher, K., 2014. Rise and fall of late Pleistocene pluvial lakes in response to reduced evaporation and precipitation: evidence from Lake Surprise, California. Bull. Geol. Soc. Am. 126, 1387–1415. https://doi.org/10.1130/B31014.1.

Kageyama, M., Harrison, S., Kapsch, M.-L., Löfverström, M., Lora, J., Mikolajewicz, U., Sherriff-Tadano, S., Vadsaria, T., Abe-Ouchi, A., Bouttes, N., Chandan, D., LeGrande, A., Lhardy, F., Lohmann, G., Morozova, P., Ohgaito, R., Peltier, W.R., Quiquet, A., Roche, D., Shi, X., Schmittner, A., Tierney, J., Volodin, E., 2021. The PMIP4-CMIP6 Last Glacial Maximum experiments: preliminary results and comparison with the PMIP3-CMIP5 simulations. Clim. Past Discuss., 1–37. https://doi.org/10.5194/cp-2019-169.

Kim, S.J., Crowley, T.J., Erickson, D.J., Govindasamy, B., Duffy, P.B., Lee, B.Y., 2008. High-resolution climate simulation of the Last Glacial Maximum. Clim. Dyn. 31, 1–16. https://doi.org/10.1007/s00382-007-0332-z.

Kirby, M.E., Feakins, S.J., Bonuso, N., Fantozzi, J.M., Hiner, C.A., 2013. Latest Pleistocene to Holocene hydroclimates from Lake Elsinore, California. Quat. Sci. Rev. https://doi.org/10.1016/j.quascirev.2013.05.023.

Kutzbach, J.E., Wright, H.E., 1985. Simulation of the climate of 18,000 years BP: results for the North American/North Atlantic/European sector and comparison with the geologic record of North America. Quat. Sci. Rev. 4, 147–187. https://doi.org/10.1016/0277-3791(85)90024-1.

Lachniet, M.S., Denniston, R.F., Asmerom, Y., Polyak, V.J., 2014. Orbital control of western North America atmospheric circulation and climate over two glacial cycles. Nat. Commun. 5. https://doi.org/10.1038/ncomms4805.

Lemons, D.R., Milligan, M.R., Chan, M.A., 1996. Paleoclimatic implications of late Pleistocene sediment yield rates for the Bonneville Basin, northern Utah. Palaeogeogr. Palaeoclimatol. Palaeoecol. 123, 147–159. https://doi.org/10.1016/0031-0182(95)00117-4.

Löfverström, M., Caballero, R., Nilsson, J., Kleman, J., 2014. Evolution of the large-scale atmospheric circulation in response to changing ice sheets over the Last Glacial Cycle. Clim. Past 10, 1453–1471. https://doi.org/10.5194/cp-10-1453-2014.

Lora, J.M., 2018. Components and mechanisms of hydrologic cycle changes over North America at the Last Glacial Maximum. J. Climate 31, 7035–7051. https://doi.org/10.1175/JCLI-D-17-0544.1.

Lora, J.M., Mitchell, J.L., Risi, C., Tripati, A.E., 2017. North Pacific atmospheric rivers and their influence on western North America at the Last Glacial Maximum. Geophys. Res. Lett. 44, 1051–1059. https://doi.org/10.1002/2016GL071541.

Lu, J., Chen, G., Frierson, D.M.W., 2008. Response of the zonal mean atmospheric circulation to El Niño versus global warming. J. Climate 21, 5835–5851. https://doi.org/10.1175/2008JCLI2200.1.

Maher, K., Ibarra, D.E., Oster, J.L., Miller, D.M., Redwine, J.L., Reheis, M.C., Harden, J.W., 2014. Uranium isotopes in soils as a proxy for past infiltration and precipitation across the western United States. Am. J. Sci. 314, 821–857. https://doi.org/10.2475/04.2014.01.

Manabe, S., Broccoli, A.J., 1985. The influence of continental ice sheets on the climate of an ice age. J. Geophys. Res. 90, 2167–2190. https://doi.org/10.1029/JD090iD01p02167.

Mantua, N.J., Hare, S.R., Zhang, Y., Wallace, J.M., Francis, R.C., 1997. A Pacific Interdecadal climate oscillation with impacts on salmon production. Bull. Am. Meteorol. Soc. 78, 1069–1079. https://doi.org/10.1175/1520-0477(1997)078<1069:APICOW>2.0.CO;2.

Morrill, C., Lowry, D.P., Hoell, A., 2018. Thermodynamic and dynamic causes of pluvial conditions during the Last Glacial Maximum in western North America. Geophys. Res. Lett. 45, 335–345. https://doi.org/10.1002/2017GL075807.

Norris, J.R., Zhang, Y., Wallace, J.M., 1998. Role of low clouds in summertime atmosphere-ocean interactions over the North Pacific. J. Climate 11, 2482–2490. https://doi.org/10.1175/1520-0442(1998)011<2482:ROLCIS>2.0.CO;2.

Oster, J.L., Ibarra, D.E., Winnick, M.J., Maher, K., 2015. Steering of westerly storms over western North America at the Last Glacial Maximum. Nat. Geosci. 8, 201–205. https://doi.org/10.1038/ngeo2365.

Otto-Bliesner, B.L., Brady, E.C., Clauzet, G., Tomas, R., Levis, S., Kothavala, Z., 2006. Last Glacial Maximum and Holocene climate in CCSM3. J. Climate 19, 2526–2544. https://doi.org/10.1175/JCLI3748.1.

Owen, L.A., Finkel, R.C., Minnich, R.A., Perez, A.E., 2003. Extreme southwestern margin of late Quaternary glaciation in North America: timing and controls. Geology 31, 729–732. https://doi.org/10.1130/G19561.1.

Qu, X., Hall, A., Klein, S.A., Caldwell, P.M., 2014. On the spread of changes in marine low cloud cover in climate model simulations of the 21st century. Clim. Dyn. 42, 2603–2626. https://doi.org/10.1007/s00382-013-1945-z.

Rae, J.W.B., Gray, W.R., Wills, R.C.J., Eisenman, I., Fitzhugh, B., Fotheringham, M., Littley, E.F.M., Rafter, P.A., Rees-Owen, R., Ridgwell, A., Taylor, B., Burke, A., 2020. Overturning circulation, nutrient limitation, and warming in the Glacial North Pacific. Sci. Adv. 6. https://doi.org/10.1126/sciadv.abd1654.

Ralph, F.M., Dettinger, M.D., 2011. Storms, floods, and the science of atmospheric rivers. Eos 92, 265–266. https://doi.org/10.1029/2011EO320001.

Reheis, M.C., Bright, J., Lund, S.P., Miller, D.M., Skipp, G., Fleck, R.J., 2012. A half-million-year record of paleoclimate from the Lake Manix Core, Mojave Desert, California. Palaeogeogr. Palaeoclimatol. Palaeoecol. 365–366, 11–37. https://doi.org/10.1016/j.palaeo.2012.09.002.

Roberts, W.H.G., Li, C., Valdes, P.J., 2019. The mechanisms that determine the response of the Northern Hemisphere's stationary waves to North American ice sheets. J. Climate 32, 3917–3940. https://doi.org/10.1175/JCLI-D-18-0586.1.

Ronca, R.E., Battisti, D.S., 1997. Anomalous sea surface temperatures and local air-sea energy exchange on intraannual timescales in the northeastern subtropical Pacific. J. Climate 10, 102–117. https://doi.org/10.1175/1520-0442(1997)010<0102:ASSTAL>2.0.CO;2.

Seltzer, A.M., Ng, J., Danskin, W.R., Kulongoski, J.T., Gannon, R.S., Stute, M., Severinghaus, J.P., 2019. Deglacial water-table decline in southern California recorded by noble gas isotopes. Nat. Commun. 10. https://doi.org/10.1038/s41467-019-13693-2.

Smith, D.M., Booth, B.B.B., Dunstone, N.J., Eade, R., Hermanson, L., Jones, G.S., Scaife, A.A., Sheen, K.L., Thompson, V., 2016. Role of volcanic and anthropogenic aerosols in the recent global surface warming slowdown. Nat. Clim. Change 6, 936–940. https://doi.org/10.1038/nclimate3058.

Tao, W., Yi, L., Wei, H., 2013. Last Glacial Maximum sea surface temperatures: a model-data comparison. Atmos. Ocean. Sci. Lett. 6, 233–239. https://doi.org/10.3878/j.issn.1674-2834.13.0019.

Thompson, R.S., Anderson, K.H., Bartlein, P.J., 1999. Quantitative paleoclimatic reconstructions from late Pleistocene plant macrofossils of the Yucca Mountain region, U.S. Geological Survey Open-File Report.

Tierney, J.E., Zhu, J., King, J., Malevich, S.B., Hakim, G.J., Poulsen, C.J., 2020. Glacial cooling and climate sensitivity revisited. Nature 584, 569–573. https://doi.org/10.1038/s41586-020-2617-x.

Ting, M., 1994. Maintenance of northern summer stationary waves in a GCM. J. Atmos. Sci. 51, 3286–3308. https://doi.org/10.1175/1520-0469(1994)051<3286:monssw>2.0.co;2.

Webb, M.J., Lambert, F.H., Gregory, J.M., 2013. Origins of differences in climate sensitivity, forcing and feedback in climate models. Clim. Dyn. 40, 677–707. https://doi.org/10.1007/s00382-012-1336-x.

Wong, C.I., Potter, G.L., Montañez, I.P., Otto-Bliesner, B.L., Behling, P., Oster, J.L., 2016. Evolution of moisture transport to the western U.S. during the last deglaciation. Geophys. Res. Lett. 43, 3468–3477. https://doi.org/10.1002/2016GL068389.

Xiao, H., Mechoso, C.R., Sun, R., Han, J., Pan, H.L., Park, S., Hannay, C., Bretherton, C., Teixeira, J., 2014. Diagnosis of the marine low cloud simulation in the NCAR community earth system model (CESM) and the NCEP global forecast system (GFS)-modular ocean model v4 (MOM4) coupled model. Clim. Dyn. 43, 737–752. https://doi.org/10.1007/s00382-014-2067-y.

Yanase, W., Abe-Ouchi, A., 2010. A numerical study on the atmospheric circulation over the midlatitude North Pacific during the Last Glacial Maximum. J. Climate 23, 135–151. https://doi.org/10.1175/2009JCLI3148.1.

# Supplementary Material for:

# Air-sea coupling shapes North American hydroclimate response to ice sheets during the Last Glacial Maximum

Dillon J. Amaya[1], Alan M. Seltzer[2], Kristopher B. Karnauskas[1,3], Juan M. Lora[4], X. Zhang[5], and Pedro N. DiNezio[3]

**[1]Cooperative Institute for Research in Environmental Sciences, University of Colorado Boulder**

**[2]Woods Hole Oceanographic Institution**

**[3]Department of Atmospheric and Oceanic Sciences, University of Colorado Boulder**

**[4]Department of Earth and Planetary Sciences, Yale University**

**[5]Department of Earth and Planetary Sciences, Johns Hopkins University**

Corresponding author: Dillon J. Amaya, dillon.amaya@colorado.edu, 816-916-8348

**This PDF file includes:**

## S1 Equilibrium mixed layer heat budget

*S1.1 Heat budget derivation*

To diagnose the physical processes that drive the main features of the sea surface temperature (SST) anomaly patterns discussed in this study, we conduct a mixed layer heat budget analysis following Xie et al. (2010). The mixed layer heat budget can be written as:

$$\rho c_p H \frac{\partial SST'}{\partial t} = Q'_{SW} + Q'_{LW} + Q'_{SH} + Q'_{LH} + O' \quad \text{(S1)}$$

where $\rho$ is ocean density, $c_p$ is the specific heat capacity of seawater, $H$ is the ocean mixed layer depth, and $SST'$ is the mixed layer temperature (estimated here as SST). Primes denote differences between our perturbed simulations (e.g., WM or GM) and the CTL simulations. The combination of terms on the left-hand side (LHS) represent time variations in the mixed layer heat storage, which is very close to zero in the annual mean of our equilibrium climate simulations (not shown). The terms on the right-hand side (RHS) represent the drivers of those changes (positive values = SST warming), which include net surface shortwave radiation ($Q'_{SW}$), net surface longwave radiation ($Q'_{LW}$), sensible ($Q'_{SH}$) and latent ($Q'_{LH}$) heat fluxes, and the heat flux due to ocean dynamics ($O'$) calculated as a residual.

We aim to rewrite Eq. (S1) as a diagnostic equation for SST anomalies between our equilibrium simulations due to the dependency of the latent heat flux on SST (Hwang et al., 2017; Jia and Wu, 2013; Zhang et al., 2020). To get there, we begin with the bulk formula for the latent heat flux:

$$Q_{LH} = -L_v c_E \rho_a W [q_s(SST) - q_a] \quad \text{(S2)}$$

where $L_v$ is the latent heat of vaporization, $c_E$ is the transfer coefficient, $\rho_a$ is the near-surface air density, $W$ is the surface wind speed, and $q_a$ is the specific humidity of air above the sea surface. The near-surface specific humidity of air is defined as:

$$q_a = RH_0 q_s(SST + \Delta T) \tag{S3}$$

where $RH_0$ is the relative humidity at the sea surface, and $\Delta T = T_a - SST$ is the near-surface temperature gradient. Using the Clausius-Clapeyron equation, Eq. (S3) can be rewritten as:

$$q_a = RH_0 q_s(SST) e^{\alpha \Delta T} \tag{S4}$$

where $\alpha = \frac{L_v}{R_v T^2} \approx 0.06\ \mathrm{K}^{-1}$. Plugging Eq. (S4) into Eq. (S2), we get:

$$Q_{LH} = -L_v c_E \rho_a W (1 - RH_0 e^{\alpha \Delta T}) q_s(\mathrm{SST}) \tag{S5}$$

Following Jia and Wu (2013), anomalies of $Q_{LH}$ can be linearized such that:

$$Q'_{LH} = \frac{\delta Q_{LH}}{\delta SST} SST' + \frac{\delta Q_{LH}}{\delta W} W' + \frac{\delta Q_{LH}}{\delta RH_0} RH'_0 + \frac{\delta LH}{\delta \Delta T} \Delta T' \tag{S6}$$

The last three terms on the RHS represent contributions to the total latent heat flux from near-surface wind speed, near-surface relative humidity, and air-sea temperature contrasts, respectively. These terms can be represented as:

$$Q_{LH,w} = \frac{\delta Q_{LH}}{\delta W} W' = \overline{Q_{LH}} \frac{W'}{\overline{W}}, \tag{S7}$$

$$Q_{LH,RH} = \frac{\delta Q_{LH}}{\delta RH_0} RH'_0 = -\frac{\overline{Q_{LH}} RH'_0}{e^{\alpha \overline{\Delta T}} - \overline{RH_0}}, \tag{S8}$$

$$Q_{LH,\Delta T} = \frac{\delta Q_{LH}}{\delta \Delta T} \Delta T' = \frac{\alpha \overline{Q_{LH}}\, \overline{RH_0} \Delta T'}{e^{\alpha \overline{\Delta T}} - \overline{RH_0}}, \tag{S9}$$

while the first term on the RHS of Eq. (S6) represents SST damping from Newtonian cooling:

$$Q_{LH,SST} = \frac{\delta Q_{LH}}{\delta SST} SST' = \alpha \overline{Q_{LH}} SST' \tag{S10}$$

where overbars denote the climatological mean. By substituting Eq. (S10) into Eq. (S1) and solving, we arrive at a diagnostic equation for $SST'$:

$$SST' = -\frac{Q'_{SW} + Q'_{LW} + Q'_{SH} + Q'_{LH,w} + Q'_{LH,RH} + Q'_{LH,\Delta T} + O'}{\alpha \overline{Q_{LH}}} \tag{S11}$$

Finally, Eq. (S11) can be rewritten to show how each forcing term contributes to $SST'$:

$$SST' = SST'_{SW} + SST'_{LW} + SST'_{SH} + SST'_O + SST'_{LH,w} + SST'_{LH,RH} + SST'_{LH,\Delta T} \tag{S12}$$

where:

$$SST'_{SW} = -\frac{Q'_{SW}}{\alpha\overline{Q_{LH}}}, \tag{S13}$$

$$SST'_{LW} = -\frac{Q'_{LW}}{\alpha\overline{Q_{LH}}}, \tag{S14}$$

$$SST'_{SH} = -\frac{Q'_{SH}}{\alpha\overline{Q_{LH}}}, \tag{S15}$$

$$SST'_{Ocn} = -\frac{O'}{\alpha\overline{Q_{LH}}}, \tag{S16}$$

$$SST'_{LH,w} = -\frac{Q'_{LH,w}}{\alpha\overline{Q_{LH}}} = -\frac{W'}{\alpha\overline{W}}, \tag{S17}$$

$$SST'_{LH,RH} = -\frac{Q'_{LH,RH}}{\alpha\overline{Q_{LH}}} = -\frac{RH'_0}{\alpha(e^{\alpha\overline{\Delta T}} - \overline{RH_0})}, \tag{S18}$$

$$SST'_{LH,\Delta T} = -\frac{Q'_{LH,\Delta T}}{\alpha\overline{Q_{LH}}} = -\frac{\overline{RH_0}\,\Delta T'}{e^{\alpha\overline{\Delta T}} - \overline{RH_0}}, \tag{S19}$$

*S1.2 Cloud parameters*

The contribution of surface shortwave radiation to $SST'$ can be further decomposed as:

$$SST'_{SW} = SST'_{SW,Cld} + SST'_{SW,Clr} \tag{S21}$$

where $SST'_{SW,Cld}$ is the SST contribution from the changes in shortwave cloud radiative forcing and $SST'_{SW,Clr}$ is the SST contribution from changes in shortwave radiation at the surface under a clear sky. The terms in Eq. (S21) are shown in Figure 7 of the main text, where the LHS is Eq. (S13) and the RHS terms are:

$$SST'_{SW,Clr} = -\frac{Q'_{SW,Clr}}{\alpha\overline{Q_{LH}}} \tag{S22}$$

$$SST'_{SW,Cld} = \frac{Q'_{SW} - Q'_{SW,Clr}}{\alpha\overline{Q_{LH}}} \tag{S23}$$

The cloud forced cooling seen in $WM_{DOM}$ and $WM_{AGCM}$ is closely mirrored by increases in summertime low cloud fraction throughout the North Pacific (Figure 8a,d). Following Scott et

al. (2020), we diagnose the physical drivers of these low cloud changes by comparing to summertime averaged Estimated Inversion Strength (EIS) and 700 mb relative humidity (RH) anomalies in each of our simulations (Figures 8b-c and 8e-f). The EIS is calculated as:

$$EIS = LTS - \Gamma_m^{850}(z_{700} - LCL) \quad \text{(S24)}$$

where *LTS* is the lower tropospheric stability and is equal to the difference between the air temperature at 700 mb and the surface temperature, $z_{700}$ is the height of the 700 mb pressure surface, *LCL* is the lifted condensation level (i.e., the cloud bottom) calculated following Georgakakos and Bras (1984), and $\Gamma_m^{850}$ is the moist adiabatic lapse rate at 850 mb calculated as:

$$\Gamma_m^{850} = \frac{g}{c_{pa}}\left[1 - \frac{1 + {L_v w_s^{850}}/{R_d T^{850}}}{1 + {L_v^2 w_s^{850}}/{c_{pa} R_v T^{850^2}}}\right] \quad \text{(S25)}$$

where $w_s^{850}$ and $T^{850}$ are the saturation mixing ratio and air temperature at 850 mb, respectively, and $R_d$ and $R_v$are the gas constants for dry air and water vapor, respectively, and $c_{pa}$ is the specific heat capacity of air at constant pressure. The EIS (˚C) is a measure of the strength of the temperature inversion above the marine boundary layer (MBL). Positive EIS values correspond to a stronger inversion and reduced mixing between the moist MBL and the drier free troposphere and are therefore highly correlated with increases in low cloud fraction Wood and Bretherton (2006).

*S1.3 Ekman heat transport*

Annual mean Ekman heat advection anomalies for GM and WM dynamical ocean model (DOM) simulations are shown in Figure S6. Anomalous Ekman heat advection ($Q'_{ek}$) is calculated following Alexander and Scott (2008):

$$Q'_{ek} = \frac{c_p}{f}\left(\tau_x \frac{\delta SST}{\delta y} - \tau_y \frac{\delta SST}{\delta x}\right) \quad \text{(S20)}$$

where $f$ is the Coriolis parameter, $\tau_x$ and $\tau_y$ are the zonal and meridional surface wind stress, and $\frac{\delta SST}{\delta x}$ and $\frac{\delta SST}{\delta y}$ are the zonal and meridional SST gradients, which we use to estimate the horizontal temperature gradients within the Ekman layer.

*S1.4 Heat budget interpretation*

The SST budgets shown in Figures S4 and S5 use Eqs. (S12-S19). As this heat budget is only valid for the upper ocean, the budget terms are only plotted for grid cells that are 100% ocean for the entire year. Grid cells that experience any fraction of seasonal sea ice are masked out. Note that these budgets are not expected to close exactly. In particular, this heat budget decomposition assumes a local quasi-equilibrium between the surface temperature and near-surface air temperature. Therefore, $SST'$ in Eq. (S12) may have larger errors in regions with strong boundary layer temperature advection, which may occur near areas with large surface temperature gradients (e.g., near sea ice, western boundary currents, etc.). There may be additional errors brought on from non-linearities in the surface heat flux terms that are not captured in our analysis.

Additionally, we note that this heat budget decomposition can only be applied for annual mean data. This is due to the necessary assumption that the mixed layer heat storage (LHS, Eq. S1) is close to zero, which is only true in the annual mean of our equilibrium climate simulations. Seasonal averages of equilibrium mixed layer heat storage are not required to be close to zero as they may be balanced by opposite signed changes in other seasons. Despite these caveats, our annual mean heat budget is a useful qualitative tool to identify the dominant SST-forcing terms, which when combined with other seasonally averaged climate anomalies (as in Figure 7g), can provide clues for the specific ocean-atmosphere interactions at play.

## S2 Influence of LGM greenhouse gas forcing

While subpolar warming is key in shaping the overall wintertime North Pacific atmospheric circulation response in our $GM_{DOM}$ simulation, this SST pattern may be less apparent when other LGM boundary conditions are also considered. For example, it may be possible that the global cooling associated with reduced LGM GHGs is enough to offset the subpolar warming seen in $GM_{DOM}$, thus making it possible for mechanical ice sheet forcing alone to drive the expected hydroclimate response. To test this, we estimate the climate response to reduced LGM GHGs using two methods: (1) A fully coupled simulation that is identical to the pre-industrial simulation except with GHGs set to PMIP3 LGM levels (referred to as $LGM_{GHG}$) and (2) The difference of $LGM_{Full}$ and our $WM_{DOM}$ simulation. The first method estimates the impact of reduced GHGs relative to modern day topography. The second method estimates the impact of reduced GHGs (with some relatively minor contributions from changes in orbital forcing) relative to LGM topography.

Regardless of the method, we find that reducing GHGs to LGM levels does not produce a North Pacific jet shift or a western North America hydroclimate response that is consistent with $LGM_{Full}$ (Figure S7a-d). Even if we assume that the climate impacts of ice sheet topography and reduced LGM GHGs are, to first order, linearly additive (as supported by Zhu and Poulsen, (2021)), their combined effects are still unable to reproduce the expected atmospheric circulation or hydroclimate response (Figure S7e-f). This is because reducing GHGs does not significantly alter the anomalous meridional temperature gradient set up by the direct mechanical ice sheet forcing in $GM_{DOM}$. Instead, reducing GHGs merely cools the North Pacific fairly uniformly (not shown), which does not significantly impact the North Pacific jet stream. This is consistent with previous studies that showed that lowered GHGs can indeed influence Northern Hemisphere

stationary waves, but that this effect is minor relative to other LGM boundary conditions (Broccoli and Manabe, 1987; Masson-Delmotte et al., 2006).

## S3 Additional AGCM experiments

In order to isolate the contribution of SST-forcing to the overall atmospheric circulation anomalies seen in coupled simulations, we conducted a series of additional CAM5 simulations (referred to as WM-SST) forced at the lower boundary with the long-term monthly mean SST output from the $WM_{DOM}$ experiment (Figure 6a). Sea ice fraction was prescribed following a repeated seasonal cycle from the $CTL_{DOM}$ simulation. Separate experiments were conducted by forcing CAM5 with $WM_{DOM}$ SSTs (a) globally, (b) in the tropics-only (20˚S-20˚N), (c) in the North Pacific-only (>30˚N), and (d) in the Northern extratropics (>30˚N, all longitudes). Grid points not prescribed with $WM_{DOM}$ SSTs were set to the CTL SST seasonal cycle. Each simulation was integrated for 40 years. Due to the short decorrelation timescale of the atmosphere, each year of these simulations was treated as a separate ensemble member. All anomalies are relative to a WM-SST control experiment forced with $CTL_{DOM}$ SSTs globally. Results are shown for the boreal winter (December-February) ensemble average within each experiment (Figure 6).

**Table S1** List of PMIP3 models used in this study. Where a model offered multiple ensemble members, only the first ensemble member was used for analysis.

| Institution | Model | Resolution (lat x lon) |
|---|---|---|
| National Center for Atmospheric Research | CCSM4 | 0.94˚ x 1.25˚ |
| Centre National de Recherches M´et´eorologiques/Centre Europ´een de Recherche et de Formation Avanc´ee en Calcul Scientifique | CNRM-CM5 | 1.4˚ x 1.4˚ |
| LASG, Institute of Atmospheric Physics, Chinese Academy of Sciences and CESS, Tsinghua University | FGOALS-g2 | 2.8˚ x 2.8˚ |
| NASA Goddard Institute for Space Studies | GISS-E2-R | 2.0˚ x 2.5˚ |
| Institut Pierre-Simon Laplace | IPSL-CM5A-LR | 1.9˚ x 3.75˚ |
| Japan Agency for Marine-Earth Science and Technology, Atmosphere and Ocean Research Institute (The University of Tokyo), and National Institute for Environmental Studies | MIROC-ESM | 2.8˚ x 2.8˚ |
| Max Planck Institute for Meteorology | MPI-ESM-P | 1.87˚ x 1.87˚ |
| Meteorological Research Institute | MRI-CGCM3 | 1.12˚ x 1.12˚ |

**Table S2** Compilation of western North American LGM minus pre-industrial precipitation difference estimates from (second column) proxy records and (third column) our CESM1 $LGM_{Full}$ simulation. Proxy locations are in the first column. Paired CESM1 data is from the nearest grid cell. Proxy estimates are modified from Lora et al. (2017). Superscripts in the second column denote the citation for each respective proxy estimate. Full references are in main text.

| Location | ΔP, Proxy Estimates (mm $day^{-1}$) | ΔP, CESM1 $LGM_{Full}$ - CTL (mm $day^{-1}$) |
|---|---|---|
| 47˚N, 123˚W | $-3.4 \pm 0.2$[1] | -1.2 |
| 45˚N, 123˚W | $-2.6 \pm 0.2$[1] | -0.6 |
| 45˚N, 121˚W | $-0.5 \pm 0.2$[1] | -0.4 |
| 41˚N, 121˚W | $0.2 \pm 0.1$[2] | 0.3 |
| 41˚N, 115˚W | $-0.0 \pm 0.2$[3] | 0.2 |
| 41˚N, 113˚W | $1.1 \pm 0.4$[4] | 0.2 |
| 41˚N, 111˚W | $0.3 \pm 0.7$[4] | 0.0 |
| 39˚N, 115˚W | $0.2 \pm 0.3$[1,3] | 0.2 |
| 37˚N, 119˚W | $0.3 \pm 0.3$[3] | 1.7 |
| 37˚N, 117˚W | $0.6 \pm 0.2$[1,3,5] | 0.6 |
| 37˚N, 115˚W | $0.0 \pm 0.2$[1] | 0.3 |
| 37˚N, 111˚W | $0.5 \pm 0.2$[1] | 0.1 |
| 37˚N, 109˚W | $-0.1 \pm 0.3$[1] | 0.1 |
| 35˚N, 111˚W | $-0.7 \pm 0.4$[1] | 0.3 |
| 35˚N, 109˚W | $2.0 \pm 0.3$[1] | 0.3 |
| 33˚N, 109˚W | $0.7 \pm 0.1$[1] | 0.4 |

[1]Bartlein et al. (2011), [2]Ibarra et al. (2014), [3]Maher et al. (2014), [4]Lemons et al. (1996), [5]Thompson et al. (1999)

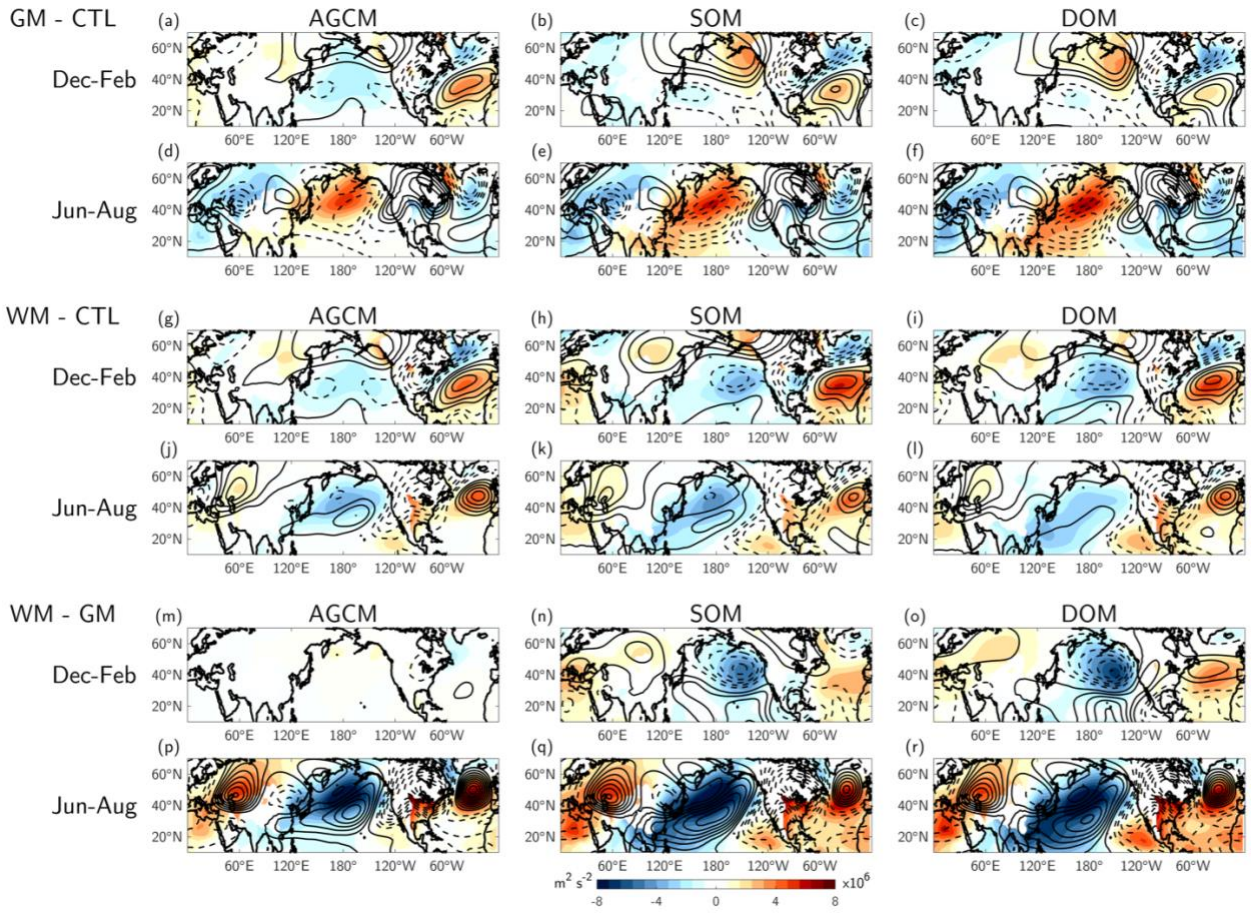


**Figure S1** Single forcing North Pacific circulation response. Geostrophic streamfunction anomalies ($m^2\ s^{-2}$) at 850 mb (shading) and 200 mb (black contours) in the GM minus CTL AGCM (left column), SOM (middle column), and DOM (right column) ocean configurations, averaged for (a)-(c) December-February and (d)-(f) June-August. Solid (dashed) black contours denote positive (negative) values. Black contour interval is $2x10^6\ m^2\ s^{-2}$ starting at $2x10^6\ m^2\ s^{-2}$.

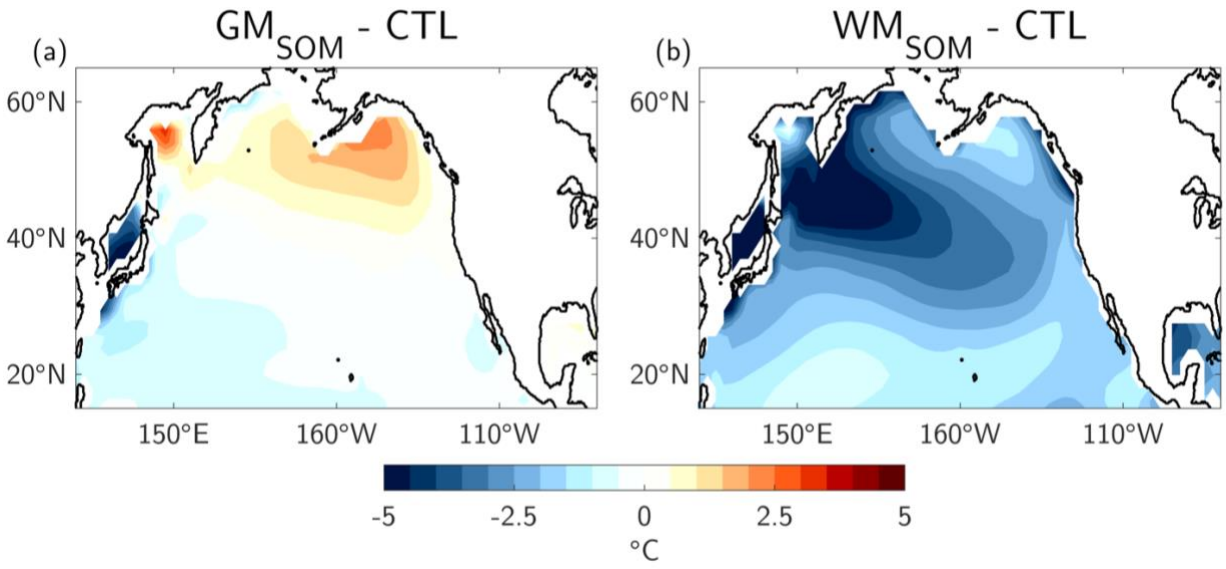


**Figure S2** Simulated ocean temperature response. Difference maps of annual mean SSTs (˚C) in (a) $GM_{SOM}$ minus CTL and (b) $WM_{SOM}$ minus CTL.

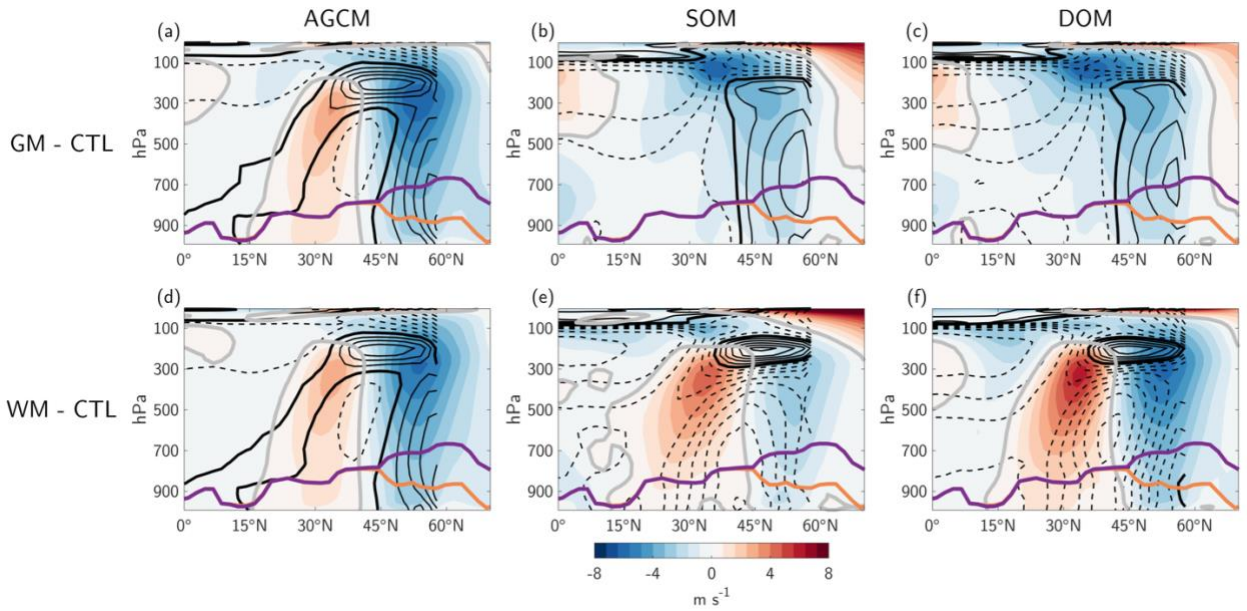


**Figure S3** North Pacific wind and temperature response. Latitude-height cross-section of boreal winter (December-February) zonal wind (shading; m $s^{-1}$) and air temperature anomalies (black contours; ˚C) in (a)-(c) each GM and (d)-(f) each WM simulation, zonally averaged over the Pacific basin (120˚E-110˚W). Temperature values are only averaged over grid cells that are 100% ocean during boreal winter (i.e., excluding grid cells with land or seasonal sea ice). Purple and orange contours roughly outline the profile of North American topography at each latitude (i.e., as if looking westward from the Atlantic Ocean) for LGM and CTL, respectively. Solid (dashed) black contours denote positive (negative) values. Black contour interval is 0.5˚C starting at 0˚C (thick black contour). Thick gray contour marks the 0 m $s^{-1}$ zonal wind anomaly contour.

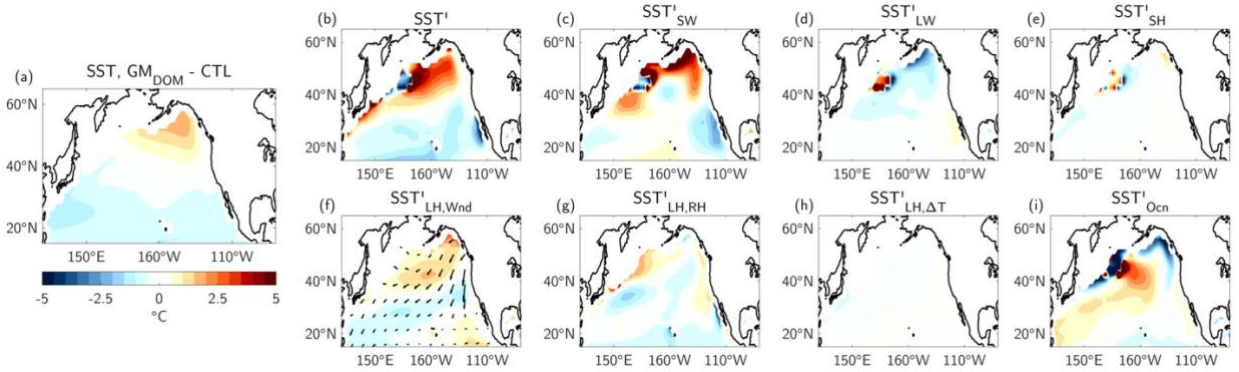


**Figure S4** GM$_{DOM}$ mixed layer heat budget. (a) Difference map of annual mean GM$_{DOM}$ minus CTL SSTs (˚C). (b)-(i) Terms of the mixed layer heat budget outlined in Eq. (S12). (b) Sum of the forcing terms, which includes contributions from (c) surface shortwave radiation, (d) surface longwave radiation, (e) the sensible heat flux, latent heat fluxes from changes in (f) wind-speed, (g) relative humidity, and (h) the air-sea temperature difference, and (i) ocean dynamical adjustments calculated as a residual. Arrows in (f) are the corresponding surface wind stress anomalies. Note that values are only shown for grid cells that are 100% ocean for the entire year (see above text on heat budget for more details).

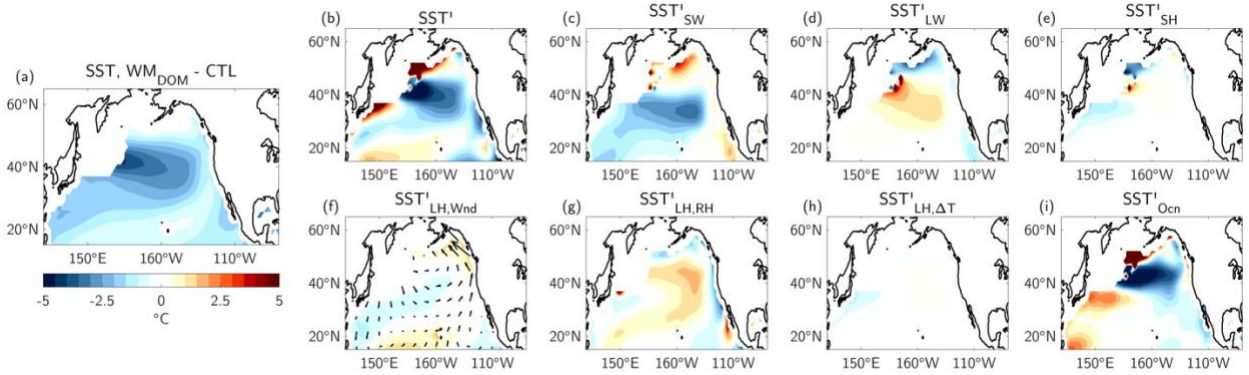


**Figure S5** WM$_{DOM}$ mixed layer heat budget. Same as Figure S4, but calculated for the WM$_{DOM}$ simulation.

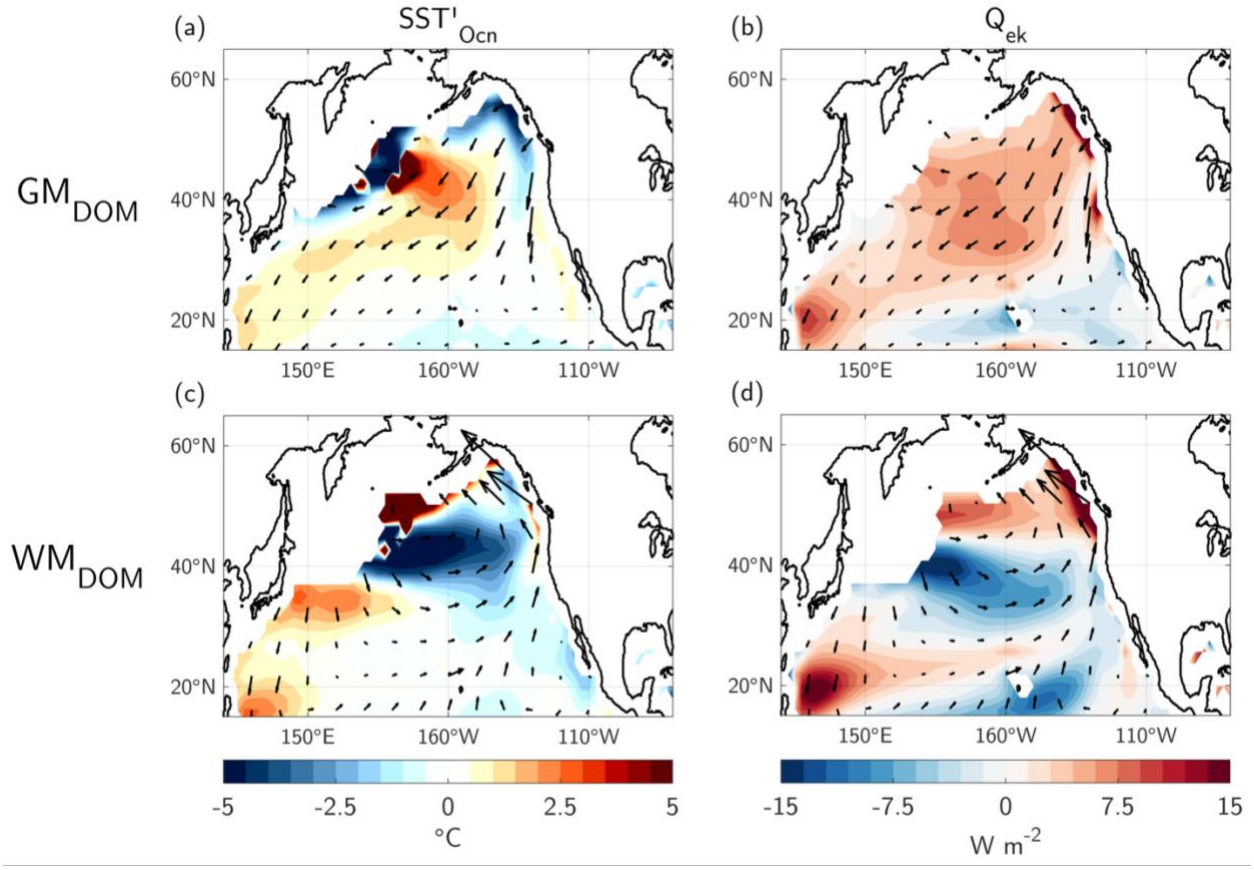


**Figure S6** Ocean circulation heat budget terms. (left column) Contribution of ocean circulation changes ($SST'_{Ocn}$; ˚C) to annual mean SST anomalies and (right column) anomalous Ekman head advection ($Q'_{ek}$; W m$^{-2}$) in (a)-(b) $GM_{DOM}$ minus CTL and (c)-(d) $WM_{DOM}$ minus CTL. Arrows show the corresponding annual mean surface wind stress anomalies.

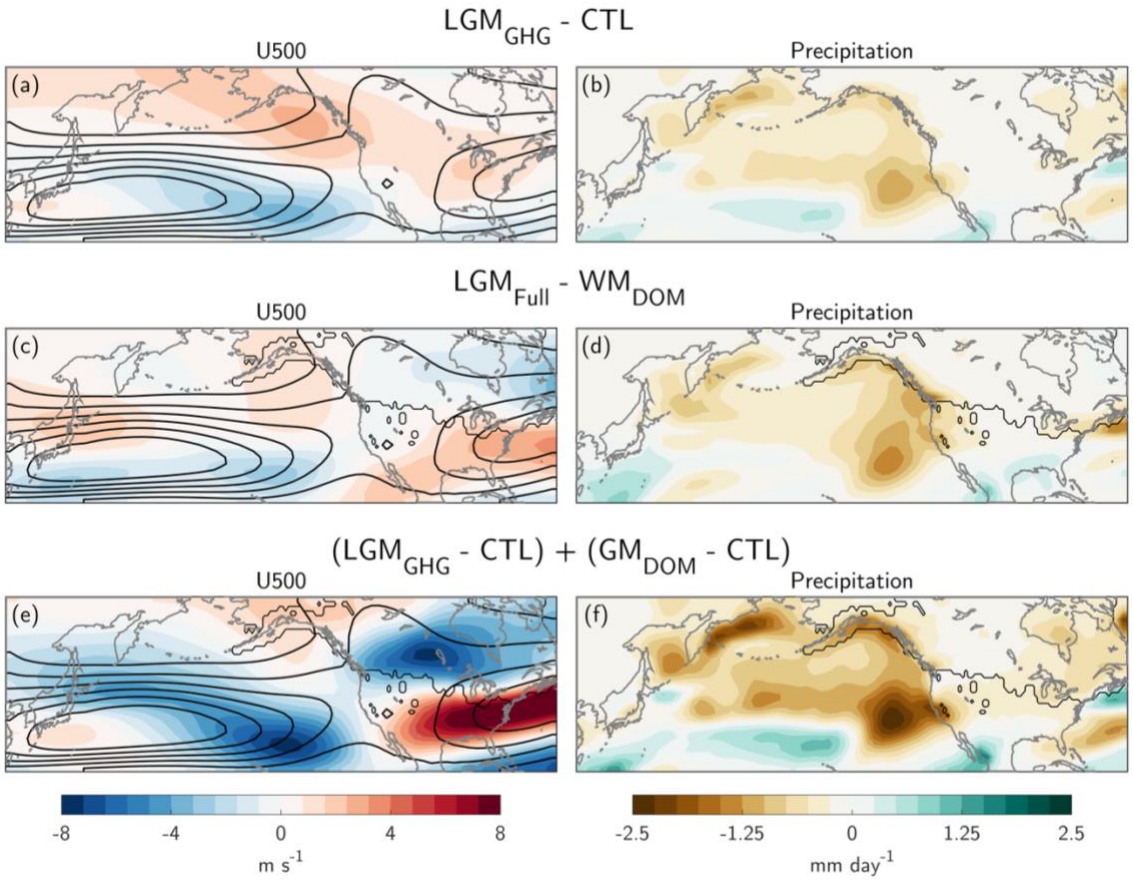


**Figure S7** Difference maps of $LGM_{GHG}$ minus CTL (a) 500 mb zonal wind (U500; m $s^{-1}$) and (b) precipitation (mm $day^{-1}$) averaged during boreal winter (December-February). (c)-(d) As in (a)-(b), but for $LGM_{Full}$ minus $WM_{DOM}$. (e)-(f) As in (a)-(b), but for the sum of $LGM_{GHG}$ minus CTL and $GM_{DOM}$ minus CTL. Thick black contours in (a) show wintertime U500 climatology in the pre-industrial control (contour interval is 5 m $s^{-1}$ with max value of 30 m $s^{-1}$). Thin black contour in (c)-(f) marks approximate ice sheet edge at the LGM.

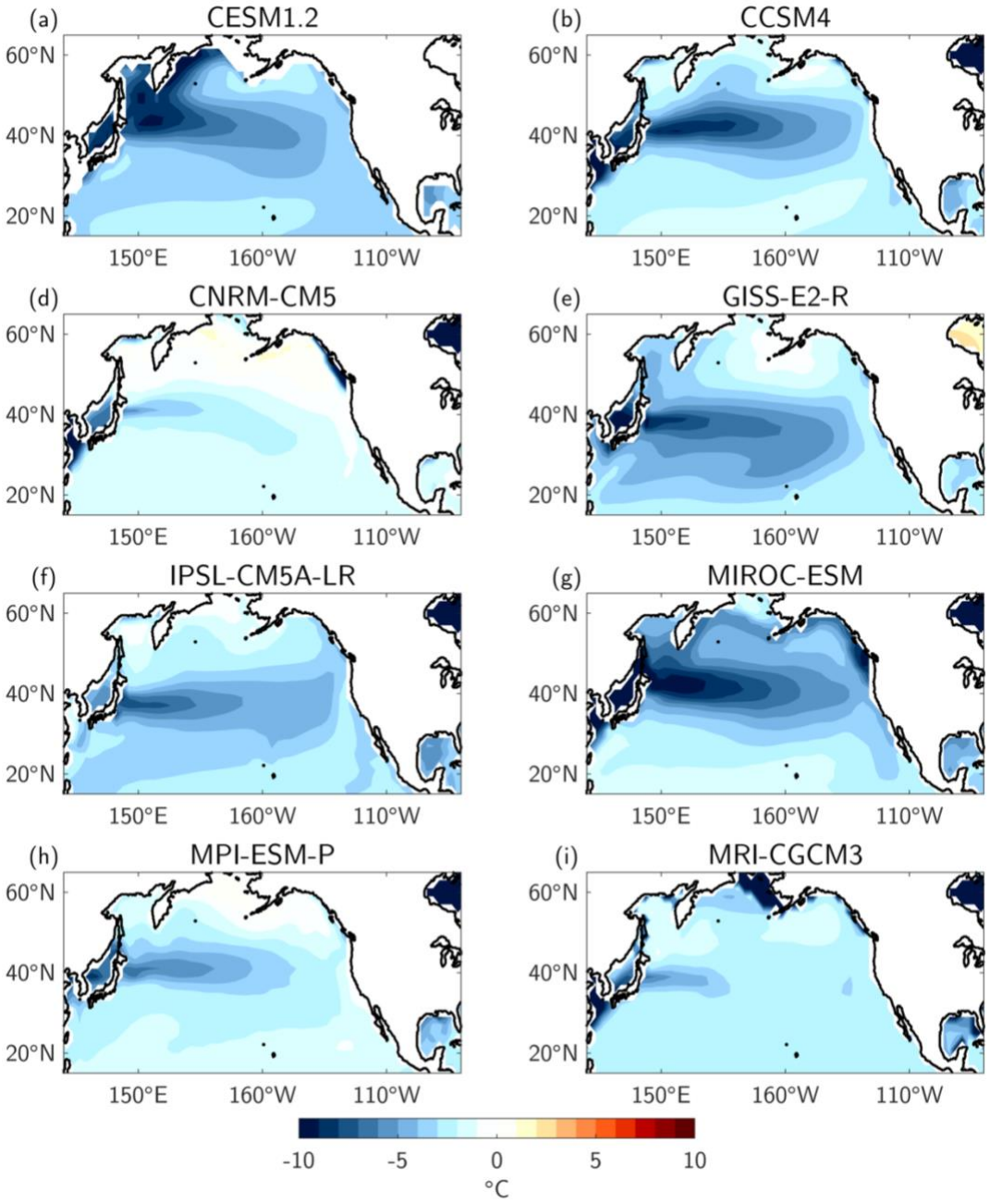


**Figure S8** Difference maps of annual mean SSTs (˚C) in (a) our CESM1 $LGM_{Full}$ minus CTL, (b)-(i) the seven $LGM_{Full}$ PMIP3 simulations minus their respective pre-industrial control simulations. The specifications for each PMIP3 model shown here are outlined in Table S1.

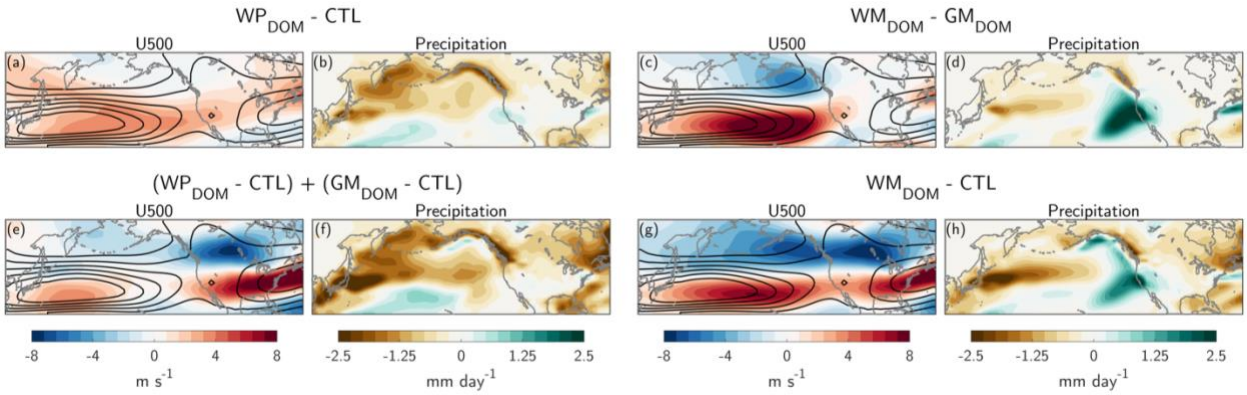


**Figure S9** Difference maps of 500mb zonal winds (U500; m $s^{-1}$) and precipitation (mm $day^{-1}$) anomalies averaged during boreal winter (December-February). Top row: impact of ice sheet albedo as estimated by (a)-(b) $WP_{DOM}$ anomalies and (c)-(d) $WM_{DOM}$ minus $GM_{DOM}$. Bottom row: combined impact of ice sheet albedo and ice sheet topography as estimated by (e)-(f) the sum of $WP_{DOM}$ and $GM_{DOM}$ anomalies and (g)-(h) $WM_{DOM}$ anomalies. Thick black contours in zonal wind plots show wintertime U500 climatology in the pre-industrial control (contour interval is 5 m $s^{-1}$ with max value of 30 m $s^{-1}$).

## References


Alexander, M.A., Scott, J.D., 2008. The role of Ekman Ocean heat transport in the northern hemisphere response to ENSO. J. Clim. 21, 5688–5707. https://doi.org/10.1175/2008JCLI2382.1

Broccoli, A.J., Manabe, S., 1987. The influence of continental ice, atmospheric CO2, and land albedo on the climate of the last glacial maximum. Clim. Dyn. 1, 87–99. https://doi.org/10.1007/BF01054478

Georgakakos, K.P., Bras, R.L., 1984. A hydrologically useful station precipitation model: 1. Formulation. Water Resour. Res. 20, 1585–1596. https://doi.org/10.1029/WR020i011p01585

Hwang, Y.T., Xie, S.P., Deser, C., Kang, S.M., 2017. Connecting tropical climate change with Southern Ocean heat uptake. Geophys. Res. Lett. 44, 9449–9457. https://doi.org/10.1002/2017GL074972

Jia, F., Wu, L., 2013. A study of response of the equatorial pacific SST to doubled-CO2 forcing in the coupled CAM-1.5-layer reduced-gravity ocean model. J. Phys. Oceanogr. 43, 1288–1300. https://doi.org/10.1175/JPO-D-12-0144.1

Masson-Delmotte, V., Kageyama, M., Braconnot, P., Charbit, S., Krinner, G., Ritz, C., Guilyardi, E., Jouzel, J., Abe-Ouchi, A., Crucifix, M., Gladstone, R.M., Hewitt, C.D., Kitoh, A., LeGrande, A.N., Marti, O., Merkel, U., Motoi, T., Ohgaito, R., Otto-Bliesner, B., Peltier, W.R., Ross, I., Valdes, P.J., Vettoretti, G., Weber, S.L., Wolk, F., Yu, Y., 2006. Past and future polar amplification of climate change: Climate model intercomparisons and ice-core constraints. Clim. Dyn. 26, 513–529. https://doi.org/10.1007/s00382-005-0081-9

Scott, R.C., Myers, T.A., Norris, J.R., Zelinka, M.D., Klein, S.A., Sun, M., Doelling, D.R., 2020. Observed sensitivity of low-cloud radiative effects to meteorological perturbations over the

global oceans. J. Clim. 33, 7717–7734. https://doi.org/10.1175/JCLI-D-19-1028.1

Wood, R., Bretherton, C.S., 2006. On the relationship between stratiform low cloud cover and lower-tropospheric stability. J. Clim. 19, 6425–6432. https://doi.org/10.1175/JCLI3988.1

Xie, S.P., Deser, C., Vecchi, G.A., Ma, J., Teng, H., Wittenberg, A.T., 2010. Global warming pattern formation: Sea surface temperature and rainfall. J. Clim. 23, 966–986. https://doi.org/10.1175/2009JCLI3329.1

Zhang, X., Deser, C., Sun, L., 2020. Is there a tropical response to recent observed Southern Ocean cooling? Geophys. Res. Lett. https://doi.org/10.1029/2020GL091235

Zhu, J., Poulsen, C.J., 2021. Last Glacial Maximum (LGM) climate forcing and ocean dynamical feedback and their implications for estimating climate sensitivity. Clim. Past 17, 253–267. https://doi.org/10.5194/cp-17-253-2021